

Functionalized Graphitic Carbon Nitrides for Environmental and Sensing Applications

Tuçe Fidan, Milad Torabfam, Qandeel Saleem, Chao Wang, Hasan Kurt, Meral Yüce, Junwang Tang,* and Mustafa Kemal Bayazit*

Graphitic carbon nitride ($g\text{-C}_3\text{N}_4$) is a metal-free semiconductor that has been widely regarded as a promising candidate for sustainable energy production or storage. In recent years, $g\text{-C}_3\text{N}_4$ has become the center of attention by virtue of its impressive properties, such as being inexpensive, easily fabricable, nontoxic, highly stable, and environment friendly. Herein, the recent research developments related to $g\text{-C}_3\text{N}_4$ are outlined, which sheds light on its future prospective. Various synthetic methods and their impact on the properties of $g\text{-C}_3\text{N}_4$ are detailed, along with discussion on frequently used characterization methods. Different approaches for $g\text{-C}_3\text{N}_4$ surface functionalization, mainly categorized under covalent and noncovalent strategies, are outlined. Moreover, the processing methods of $g\text{-C}_3\text{N}_4$, such as $g\text{-C}_3\text{N}_4$ -based thin films, hierarchical, and hybrid structures, are explored. Next, compared with the extensively studied energy-related applications of the modified $g\text{-C}_3\text{N}_4$ s, relatively less-examined areas, such as environmental and sensing, are presented. By highlighting the strong potential of these materials and the existing research gaps, new researchers are encouraged to produce functional $g\text{-C}_3\text{N}_4$ -based materials using diverse surface modification and processing routes.

are most extensively used in energy and storage applications: carbon, nitrogen, and hydrogen.

Due to its metal-free, polymeric nature, $g\text{-C}_3\text{N}_4$ is the most encouraging visible-light active photocatalyst. Being an inexpensive, environment-friendly, organic semiconductor^[2] (≈ 2.7 eV bandgap), $g\text{-C}_3\text{N}_4$ can successfully replace the expensive and hazardous metal-containing photocatalysts with a wide bandgap.

As shown in **Figure 1**, the structure of $g\text{-C}_3\text{N}_4$ primarily consists of carbon and nitrogen atoms, the two most prominent elements, and contains various functional moieties such as pi-bonds, Lewis basic functions, Brønsted basic functions, and H-bonding motifs. For example, NH_2 and NH groups present in the structure act as edge defects and serve as key sites for CO_2 activation, conversion, and active group catalyzation.^[3]


By virtue of its tri-s-triazine ring structure and a high degree of condensation, $g\text{-C}_3\text{N}_4$ possesses excellent thermostability, i.e., up to 600°C in air, and outstanding chemical resistance in a range of acidic and alkaline environments, such as water, tetrahydrofuran (THF), ethanol, diethyl ether, toluene solutions, and oxidizing conditions.^[1,4] However, there are two exceptions: treatment with alkali hydroxides in the molten form causes hydrolysis of the structure, whereas interaction with concentrated acids leads to

1. Introduction

Graphitic carbon nitride ($g\text{-C}_3\text{N}_4$), with its graphite-like structure and commendable stability under ambient conditions, has gained tremendous prominence among all other allotropes of C_3N_4 , such as $\alpha\text{-C}_3\text{N}_4$, $\beta\text{-C}_3\text{N}_4$, cubic- C_3N_4 , and pseudocubic- C_3N_4 .^[1] It is composed of three earth-abundant elements which

T. Fidan, M. Torabfam, Q. Saleem, M. Yüce, Dr. M. K. Bayazit
Sabanci University Nanotechnology Research and Application Center
Tuzla, İstanbul 34956, Turkey
E-mail: mkbayazit@sabanciuniv.edu

C. Wang, Prof. J. Tang
Department of Chemical Engineering
UCL
Torrington Place, London WC1E 7JE, UK
E-mail: junwang.tang@ucl.ac.uk

 The ORCID identification number(s) for the author(s) of this article can be found under <https://doi.org/10.1002/aesr.202000073>.

© 2021 The Authors. Advanced Energy and Sustainability Research published by Wiley-VCH GmbH. This is an open access article under the terms of the Creative Commons Attribution License, which permits use, distribution and reproduction in any medium, provided the original work is properly cited.

DOI: 10.1002/aesr.202000073

Dr. H. Kurt
Department of Biomedical Engineering
School of Engineering and Natural Sciences
Istanbul Medipol University
34810 Istanbul, Turkey

Dr. H. Kurt
Research Institute for Health Sciences and Technologies (SABITA)
Istanbul Medipol University
34810 Istanbul, Turkey

Dr. H. Kurt
Nanosolar Plasmonics Ltd.
Kocaeli 41400, Turkey

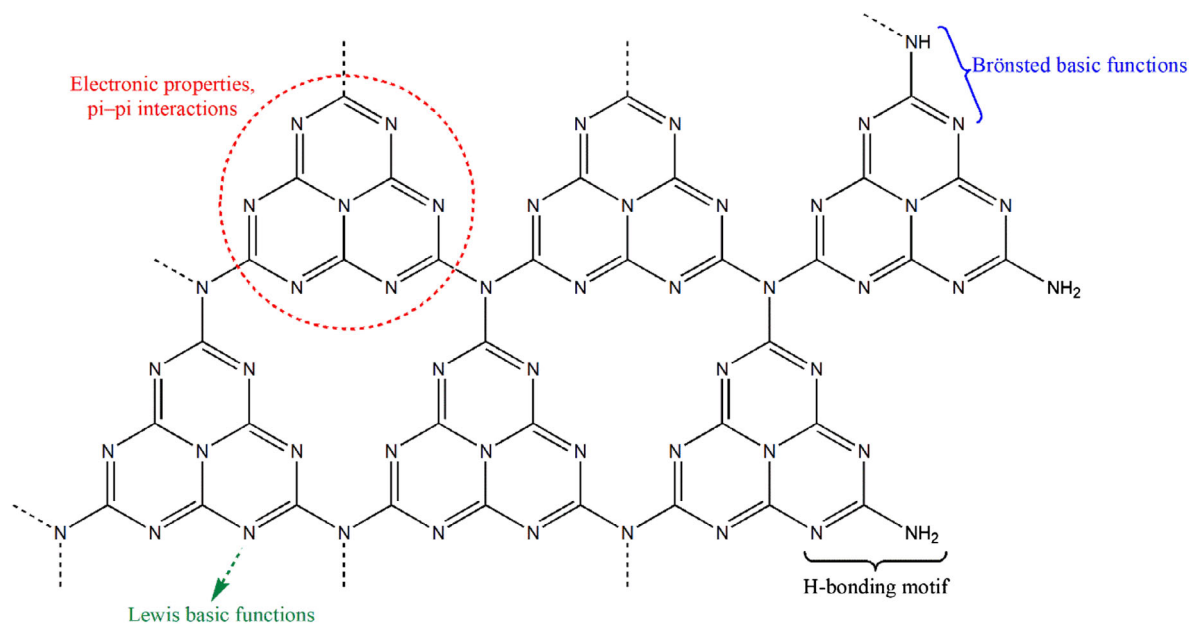


Figure 1. The structure of $g\text{-C}_3\text{N}_4$ and its functional moieties. Adapted with permission.^[3] Copyright 2014, the Royal Society of Chemistry.

colloidal, seemingly sheet-like, but fully reversible dissolution.^[5] The surface area of exfoliated $g\text{-C}_3\text{N}_4$ nanosheets (CNNSs) is much larger than the bulk C_3N_4 , which offers numerous advantages like better mass transfer during the reaction, a higher number of active sites, and improved material performance. The morphology and chemical composition of $g\text{-C}_3\text{N}_4$ can be modified by controlling the thermal treatment time.^[6] The elemental build-up, in-plane holes, and small pore size of $g\text{-C}_3\text{N}_4$ predominantly improve its optical properties and enhance its photocatalytic activity.^[7] Electron delocalization occurs throughout π -network of $g\text{-C}_3\text{N}_4$ and leads to the merger of electrons and holes, which will be consumed in reduction and oxidation reactions, respectively. As a result, the photocatalytic activity experiences a boost. As the typical absorption edge for $g\text{-C}_3\text{N}_4$ is around 450 nm, only limited solar energy can be utilized during photocatalytic reactions driven by $g\text{-C}_3\text{N}_4$. Better optical properties can be obtained by fine-tuning the electronic structure of $g\text{-C}_3\text{N}_4$ through functionalization of $-\text{NH}-$, $=\text{N}-$, $-\text{NH}_2$ groups existing on the surface. The ion-doped lattice functionalization of $g\text{-C}_3\text{N}_4$ with metal ions is found to bring a significant improvement in the properties,^[8] which is extremely beneficial for applications like hydrogen production.

Structure and surface functionalization fundamentally enhance the electronic properties, effective charge transfer, optical absorption, and photocatalytic behaviors. Elemental doping with metals and nonmetals, combining with particles, makes C_3N_4 an efficient candidate, especially for environmental applications such as water splitting and CO_2 reduction. The copolymerization and compositing with metal oxides are applied to the C_3N_4 , to provide longer cycle life and electrochemical efficiency for sensing and energy storage.

Different surface functionalization techniques are used to alter the surface area, enhance charge separation, and increase the photocatalytic efficiency of C_3N_4 . A significant amount of

research work has been dedicated to the functionalization of $g\text{-C}_3\text{N}_4$ with a range of functional materials, like carbon nanotubes (CNTs),^[9] graphene,^[10] and metal atoms,^[11]

There are many review articles on this emerging polymer's application, mainly in the energy area.^[12] Complementary to these, the critical review focuses on materials domain, including structural modification of C_3N_4 by covalent functionalization methods (e.g., reductions, oxidations, cycloadditions, cross-coupling reactions, and copolymerizations) and noncovalent ones (e.g., the interaction of organic molecules and nanoparticles with $g\text{-C}_3\text{N}_4$ surface). In addition, elemental doping to the $g\text{-C}_3\text{N}_4$ was also described. Processing bulk and functionalized $g\text{-C}_3\text{N}_4$ s to prepare thin films, hierarchical assemblies, and hybrid structures with carbonaceous materials (e.g., nanotube/ $g\text{-C}_3\text{N}_4$, graphene/ $g\text{-C}_3\text{N}_4$) has been detailed to give a postsynthesis perspective. Finally, typical examples of environmental and sensing applications of the functionalized $g\text{-C}_3\text{N}_4$ s have been discussed to emphasize the effect of functionalization.

2. Synthesis of $g\text{-C}_3\text{N}_4$

The most common method to synthesize $g\text{-C}_3\text{N}_4$ involves heating precursors with high nitrogen content, such as melamine,^[13] cyanamide,^[14] dicyandiamide (DCDA),^[15] urea,^[16] and thio-urea^[17] at elevated temperatures (usually $>500^\circ\text{C}$). The key synthetic parameters that can fine-tune the optical and electronic properties of $g\text{-C}_3\text{N}_4$ are: heating rate, precursor type, thermal treatment temperature, time, and atmosphere. Moreover, powdering the sample between heat treatment and washing procedure helps remove impurities. It should also be noted that the extraordinary chemical resistance of $g\text{-C}_3\text{N}_4$ makes the washing procedure easier. It is essential to select the temperature for synthesis carefully as it can directly affect the porosity, surface area,

composition, degree of crystallinity and polymerization, photoluminescence, and the number of active groups in the sample.^[18]

Urea is one of the most commonly used precursors due to its chemical composition (contains C, N, O, and H only), low price, and scalability. For instance, g-C₃N₄ powders were prepared by Yao et al. via direct pyrolysis of urea.^[19] A known amount of precursor was kept in four covered corundum boats and heated at 520, 550, 580, and 610 °C for 4 h, respectively, to understand the effect of the temperature. A similar route was followed by Wang et al. for the preparation of highly porous g-C₃N₄ with melamine.^[20] They heated 5 g of melamine in a muffle furnace at 550 °C for 4 h under air at a rate of 10 °C min⁻¹ and collected the yellow-colored product after cooling. They also carried out thermal copolymerization by mixing 2 g of melamine with different amounts of nucleobases, i.e., uracil, adenine, cytosine, guanine, and thymine. Zhao et al. used a fractional thermal polymerization method and produced g-C₃N₄ from melamine, DCDA, and guanidine carbonate.^[21]

Other synthetic methods discussed in the literature include one-step electrochemical synthesis^[2] and synthesis of porous g-C₃N₄ via direct polymerization.^[22] The former proposed a single-step electrochemical synthesis method to produce ultrathin g-C₃N₄ sheets. It involved the electrolysis of melamine and NaOH mixture solution for 40 min. This method was more straightforward and faster than the multistep thermal treatment method as the reaction time was highly reduced. The CNNSs produced through this method were successfully used for H₂O₂ and uric acid detection. Direct polymerization route reported a convenient route to obtain g-C₃N₄ from urea with self-supported gas. The generated gas played an essential role in the formation of pores during condensation. The products of this synthetic method were also compared with those obtained using urea-polymerized thiourea and DCDA as a source. The pyrolysis with urea produced less condensed and more porous g-C₃N₄ with better hydrogen evolution capability. As the catalytic efficiency of g-C₃N₄ depends on its porosity and surface area, the developed products were found as efficient catalysts.

While being widely used, conventional synthesis methods produce dense bulk g-C₃N₄, which has a low surface area. To increase the accessible surface area, g-C₃N₄ can be exfoliated by breaking the weak interactions between the layers of polymerized tri-s-triazine structures. Bulk g-C₃N₄ can be exfoliated into 2D nanosheets (NSs) thermally,^[23] ultrasonically,^[24] and chemically.^[25] For instance, Hatami et al. produced exfoliated NSs by dissolving 0.05 g of bulk g-C₃N₄ (prepared via pyrolysis of melamine at 600 °C for 2 h) in 50 mL of water and carrying out ultrasonication for 10 h to obtain a clear solution and, the obtained suspension was then subjected to centrifugation at 5000 rpm to get rid of unexfoliated material.^[26] In addition, some studies^[27] reported in situ fabrication of g-C₃N₄-based composites by pre-mixing the starting materials and then heating them in a furnace at around 550 °C.

Moreover, to counter the limitation of high density and introduce porosity into g-C₃N₄ materials, soft-templating and hard-templating were used.^[28] Soft templating^[29] involves self-assembling amphiphilic molecules that facilitate the formation of intricate structures by combining with precursors. In soft-templating, solvent plays a vital role in defining key characteristics of the fabricated materials, such as size and shape. On the

other hand, hard templating, also known as nanocasting method, involves deposition of precursor on a hard template.^[30] The precursor is treated to flow into the microchannels of the template and the template is removed in the end to reveal the final porous product. Hard template methods are easier to control than the soft template ones.^[28] Recently, a template-free method has also been proposed by Zhou et al. for the large-scale synthesis of 1D g-C₃N₄ microtubes.^[31] This simple method involved hydrothermal treatment of melamine precursor, which yielded white melamine-cyanuric acid microrods. The obtained microrods were pyrolyzed at 550 °C for 4 h under N₂ flow. This method was found to produce g-C₃N₄ microtubes with superior photocatalytic H₂ production. Moreover, some g-C₃N₄ synthesis routes reported in the literature are shown in **Table 1**.^[2,18–21,26,27,31,32,24b]

3. Characterization Methods

The performance of the g-C₃N₄ in various applications relies on its intrinsic properties. Hence, it is extremely crucial to enlighten the structure and electronic properties of the g-C₃N₄ fully. Various spectroscopic and microscopic techniques are available for the characterization of g-C₃N₄. Ultraviolet–visible diffuse reflectance spectroscopy (UV–vis DRS) is a useful tool to evaluate the light absorption and estimate the bandgap energy of the g-C₃N₄ through the absorption edge. Raman spectroscopy is an informative technique to evaluate the primary peaks of g-C₃N₄ corresponding with the dominant C–N stretching vibrations. X-ray photoelectron spectroscopy (XPS) facilitates the examination of the chemical states at the surface of g-C₃N₄. X-ray diffraction (XRD) is an acknowledged technique to investigate the structure and the distance between the layers of the produced g-C₃N₄. For accurate surface area measurement, Brunauer–Emmett–Teller (BET) surface area analysis is a favorable technique. Scanning electron microscopy (SEM) with energy dispersive X-ray analysis (EDX) is preferred to study the surface topography and composition of g-C₃N₄.

3.1. Ultraviolet–Visible Diffuse Reflectance Spectroscopy

Bandgap, being a predictor of the wavelength of light that a material can absorb, is a critically important property for materials in energy and environment-related applications. A decrease in bandgap energy is often associated with the red shift in the optical response of a material. UV–vis DRS is widely used to detect the bandgap of g-C₃N₄. The graph obtained from the UV–vis DRS, known as the absorption spectrum, indicates the range of wavelengths of light absorbed by a semiconductor. The spectral data, including the cut off wavelength (with the minimum absorbance value), is used to work out the bandgap energy. Moreover, the absorption capability of g-C₃N₄ is affected by the composition, defects, morphology, structure, and thickness (in the case of films) of g-C₃N₄. g-C₃N₄ film with a greater thickness (126 nm) absorbs light with longer wavelength and has a narrower bandgap than the g-C₃N₄ with a lower thickness (55 nm) (**Figure 2a**).^[33]

Moreover, N-defects formed at higher temperatures during calcination, lead to an extension in the UV–vis absorption

Table 1. Some g-C₃N₄ synthesis methods.

Synthesis method	Product	Precursors	Brief description	Ref.
Thermal condensation method	Bulk g-C ₃ N ₄	Urea, melamine, thiourea, cyanamide, and DCDA	A weighed amount of precursor was kept in a covered crucible (preferably alumina) and subjected to furnace heating at a temperature within 500–600 °C for up to 4 h. The recovered yellow residue was cooled to room temperature and ground into powder. The temperatures for different precursors are urea (550 °C), melamine (500–580 °C), thiourea (450–650 °C), cyanamide (550 °C), and DCDA (550 °C).	[18–20,26,32a]
Fractional thermal polymerization method	g-C ₃ N ₄ powder	Melamine, guanidine carbonate, and DCDA	A covered crucible containing the precursors was heated from 20 to 360 °C at a rate of 5 °C min ⁻¹ . The temperature was kept at 360 °C for 30 min and then increased again to a predetermined value within 30 min and kept there for 3 h. This was followed by cooling.	[21]
Pyrolysis-assisted chemical vapor deposition method	Free-standing g-C ₃ N ₄ films	DCDA	The precursor was contained in a quartz tube with its inlet attached to Ar flow and outlet attached to vacuum to maintain a low pressure of about 3 Torr in the tube. This arrangement caused the precursor vapors to enter the furnace (at 600 °C). Upon thermal condensation, the vapors coated the walls of the tube. The tube was then cooled to room temperature, the deposition was scraped off and a uniform free-standing film was obtained.	[32b]
Soft-template method with thermal polymerization	Exfoliated g-C ₃ N ₄	Urea	About 10 g of urea was dissolved in ethanol and water taken in 1:1 ratio, heated up to 110 °C with constant stirring. The solvent evaporated and a white precipitate was obtained. It was then transferred into a crucible and covered with aluminum foil. The crucible was heated at 550 °C for 3 h. The obtained bulk material was then dissolved in ethanol/water again and sonicated for 8 h. After centrifugation, the product was oven dried.	[24b]
Template-free solvothermal approach with post-calcination	Hierarchical nanoporous g-C ₃ N ₄ microspheres	Cyanuric chloride and melamine	The precursors were mixed in a fixed ratio and dissolved in ACN, which served as a solvent. This mixture was stirred for hours at room temperature and then placed into a Teflon-lined autoclave with a 100 mL capacity. The system was sealed and heated at a particular temperature (120–200 °C) for 12–24 h. Upon cooling, the products were centrifuged, washed with ionized water and absolute ethanol, and dried. The postcalcination treatment involved heating the sample at 550 °C in air for 4 h or Ar for 2 h.	[32c–e]
Template-free hydrothermal-assisted thermal polymerization method	1D g-C ₃ N ₄ microtubes	Melamine	Melamine precursor (0.5 g) was mixed into pure water (30 mL). The mixture was heated at 90 °C for 10 min with continuous stirring until a clear solution was obtained. The as-obtained melamine clear solution 180 °C for a day in a 50 mL Teflon stainless autoclave. The white residue was dried and calcined at 550 °C for 4 h under nitrogen. The yellowish product was collected after cooling.	[31]
Solvent-free solid reaction	g-C ₃ N ₄ powder	Cyanuric chloride and melamine	Weighed quantities of precursors (20.0 mmol cyanuric chloride and 10.0 mmol melamine) were mixed and placed into a 50 mL stainless steel autoclave. About 1 g Nickel powder was added to the precursors and the autoclave was sealed and heated up to 400 °C for 6 h. After cooling to ambient temperature, the product was washed and dried.	[32f]
Chemical vapor deposition method	Ordered cubic mesoporous g-C ₃ N ₄	Melamine	About 6 g of precursor was kept inside a 50 mL alumina crucible and KIT-6 template (2 g) was uniformly dispersed onto the precursor layer. The closed crucible was heated in a muffle furnace at 320 °C for 4 h. Upon evaporation, the precursor will be deposited into the template's pores. Next, the temperature was elevated and maintained at 550 °C for 3 h. The silica template was removed by HF acid wash and ordered cubic mesoporous g-C ₃ N ₄ were obtained.	[32g]
Microwave-assisted polymerization	g-C ₃ N ₄ sub-microspheres	Cyanuric chloride and sodium azide	The precursors were weighed (cyanuric chloride: 1.84 g and sodium azide powder: 1.96 g) and manually mixed and ground using agate mortar. The mixture was added to 40 mL of ACN solvent and stirred for 15 min. The prepared suspension was filled into a TFM vessel and placed into the cavity of a microwave system with was heated at a power of 350 W, up to 180 °C and held there for 30 min. The irradiated mixture was cooled and passed from a microfiltration membrane (pore size: 0.1 μm). The precipitate was collected and sequentially washed with ethanol, acetone, and distilled water. The sample was oven-dried at 80 °C overnight under vacuum.	[32h]

Table 1. Continued.

Synthesis method	Product	Precursors	Brief description	Ref.
One-step electrochemical method	Ultrathin CNNSs	Melamine	An electrolyte solution of 3 g melamine and 1 g NaOH was prepared in 50 mL of water. Two 4 × 4 cm ² platinum sheets were taken as electrodes and kept 0.5 cm apart. Using a DC power supply, 5 V potential was applied and the electrolysis was carried out with constant stirring for 40 min. As the mixture turned yellow, centrifugation was conducted at 10 000 rpm for 15 min. Finally, it was dialyzed for 3 days to obtain the final product.	[2]
One-step pyrolysis method	BC/g-C ₃ N ₄ composites	Urea and Hickory chips	Urea and biomass were mixed in different ratios (25:1, 50:1, and 100:1) and placed into alumina crucibles, which were covered and heated in a muffle furnace at a rate of 5 °C min ⁻¹ under air until it reached 520 °C. The temperature was maintained for 2 h and then cooled to room temperature. The products were washed with distilled water and ethanol and dried at 80 °C.	[27a]
	g-C ₃ N ₄ /Cu ₃ [Fe(CN) ₆] ₂ composite	Melamine and Cu ₃ [Fe(CN) ₆] ₂	About 2 g of HCl-treated melamine was mixed with 1 g of pre-prepared Cu ₃ [Fe(CN) ₆] ₂ powder. The mixture was dissolved in 50 mL absolute ethanol with continuous stirring for a couple of hours. The solution was heated up to 60 °C to remove ethanol and then placed in a crucible. This was followed by pyrolysis under nitrogen in a tube furnace at a 550 °C for 4 h. Upon cooling, the product was washed and dried.	[27b]

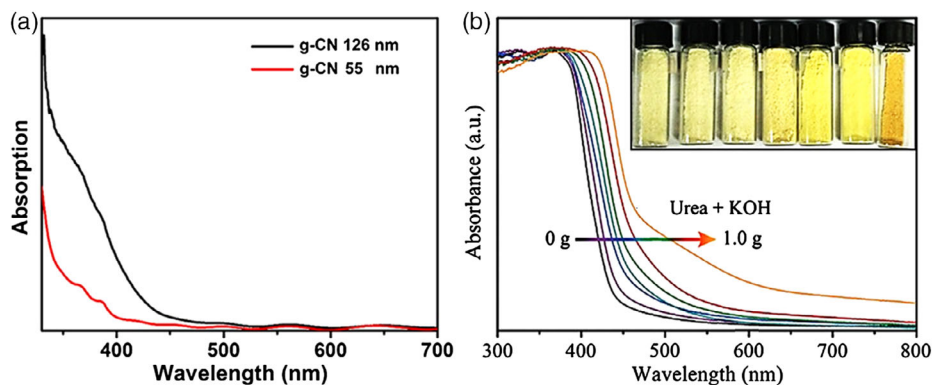


Figure 2. UV-vis spectra of g-C₃N₄ with different a) thickness and b) N-defect composition. a) Reproduced with permission.^[33] Copyright 2016, Wiley-VCH GmbH. b) Adapted with permission.^[35] Copyright 2017, Wiley-VCH GmbH.

spectra of g-C₃N₄.^[34] The absorption capability of the defective g-C₃N₄ with different N-defect concentrations, which are produced using various amounts of alkali precursor during the polymerization reaction can be increased by maintaining the bandgap energy within the range of 2.3–2.7 eV (Figure 2b). The spectra show that the g-C₃N₄ produced by this synthetic method has strong band-to-band absorption. Although, based UV-vis DRS characterizations, it is deduced that the advanced one-step in situ calcination suggests a change in the structure of g-C₃N₄, other advanced techniques such as XPS are necessary to reveal the presence of N-defects in the bulk as well as on the surface.^[35]

3.2. Raman Spectroscopy

Raman spectroscopy is a useful tool to detect vibrational, rotational, and other states in a molecular system. This technique

is also applied to study the chemical structures of g-C₃N₄. Praus and coworkers discussed the Raman spectra of the g-C₃N₄ produced via the thermal treatment of melamine at a range of temperatures. The spectra observed within 1250–400 cm⁻¹ correspond to the skeletal vibrations of nitrogen aromatic rings. The triazine skeletal vibration is visible at 980 cm⁻¹, and it is common for all samples. The typical melem bands can be seen at 1153 cm⁻¹ and 548 cm⁻¹. The highest peak was observed in samples polymerized at 550 °C and 600 °C, which signifies the complete condensation of melem given to g-C₃N₄ and its resulting decomposition at 700 °C (Figure 3).^[6]

3.3. X-Ray Diffraction

XRD is a powerful tool to study the phase structure of crystalline solids. This technique enables the identification of the crystalline

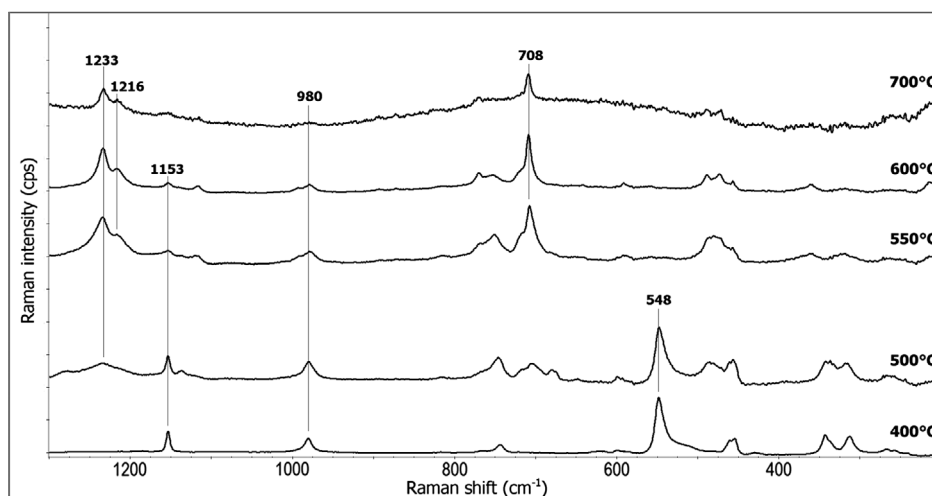


Figure 3. The Raman spectra of bulk melamine $g\text{-C}_3\text{N}_4$, produced at 400, 500, 550, 600, and 700 °C, respectively. Reproduced with permission.^[6] Copyright 2017, Elsevier.

phase and interlayer stacking planes in $g\text{-C}_3\text{N}_4$. The governing equations given below, namely Bragg's Law (Equation 1), and Scherrer equation (Equation 2) are utilized to calculate interplanar distance (d) and crystallites size (L), respectively.^[36]

$$\sin \theta = \frac{n\lambda}{2d} \quad (1)$$

$$L = \frac{K\lambda}{\beta \cos \theta} \quad (2)$$

where θ stands for the peak position (radian), n is a positive integer, λ signifies the wavelength of the source X-ray (nm), and d is the interplanar distance (nm). L represents the crystallites size (nm), K is Scherrer constant, and β is the full width of half maximum (FWHM).

For the $g\text{-C}_3\text{N}_4$, the weak diffraction peak at $\approx 13.1^\circ$ signifies (1 0 0) lattice planes of triazine units, whereas the sharp diffraction peak at $\approx 27.6^\circ$ is caused by the (0 0 2) lattice planes of interlayer stacking of aromatic segments. However, the shape, intensity, and position of these peaks can vary depending on the synthetic procedures and the surface functionalization. For example, the $g\text{-C}_3\text{N}_4$ samples produced using oxygen-containing urea showed low crystallinity compared with the ones produced by DCDA and melamine under air and nitrogen atmosphere (Figure 4a).^[37] In addition, changing the gaseous environment (air or nitrogen) had no significant effects on the XRD results. XRD was also used to investigate the defects in the structure of $g\text{-C}_3\text{N}_4$. In general, strong oxidizers can create defects in the $g\text{-C}_3\text{N}_4$ structure. A particular example was the use of H_2O_2 (a mild oxidizer) to generate hydroxyl groups on the surface.^[38] In general, strong oxidizers can create defects in the $g\text{-C}_3\text{N}_4$ structure. A particular example was the use of H_2O_2 (a mild oxidizer) to generate hydroxyl groups on the surface.^[38] As a result of hydroxylation, the characteristic (0 0 2) peak at $\approx 27.2^\circ$ shifted to higher 2θ values and the intensity of the peak increased. The observed shift and peak enhancement

were dependent on the concentration of H_2O_2 (0, 10, 20 and 30 wt%) (Figure 4b).

3.4. Other Characterization Techniques

In addition to the aforementioned characterization techniques, XPS is usually used to characterize the surface chemistry, composition, and bonding states of both the $g\text{-C}_3\text{N}_4$ and its composites.^[39] The results obtained through this spectroscopic analysis shed light on the elemental composition of a compound as well as the chemical environment of each component. However, when possible bonding configurations of N and C combine with the unavoidable interaction with the atmospheric gases (e.g., oxygen and hydrogen), interpretation of the acquired spectra become challenging.^[40]

SEM is another prominent technique that utilizes a focused electron beam to scan the surface of a sample and produce an image that provides invaluable information about the microstructure, surface properties, topography, and composition of the sample. In most cases, the surface of $g\text{-C}_3\text{N}_4$ is decorated with other materials (e.g., metal/metal oxide particles) and the information regarding the distribution, uniformity, and composition of these components can be acquired when SEM is coupled with EDX.^[41] BET surface area analysis is useful to measure the specific surface area of material by investigation of the physical adsorption of gas molecules on the $g\text{-C}_3\text{N}_4$ surface. It also provides the information of surface porosity which is highly related to the precursor type and synthesis conditions.^[42] Although the molecular formula of as-synthesized carbon nitride is represented by C_3N_4 (as a ratio of C to N), the presence of uncondensed terminal groups bearing O and/or H moieties should not be disregarded. However, due to the limitation of the characterization techniques available, it is difficult to get the real bulk structure of the so-called carbon nitrides. On the other hand, creating the characterization roadmap and progressing by considering the obtained results will be quite productive. Also, to ensure

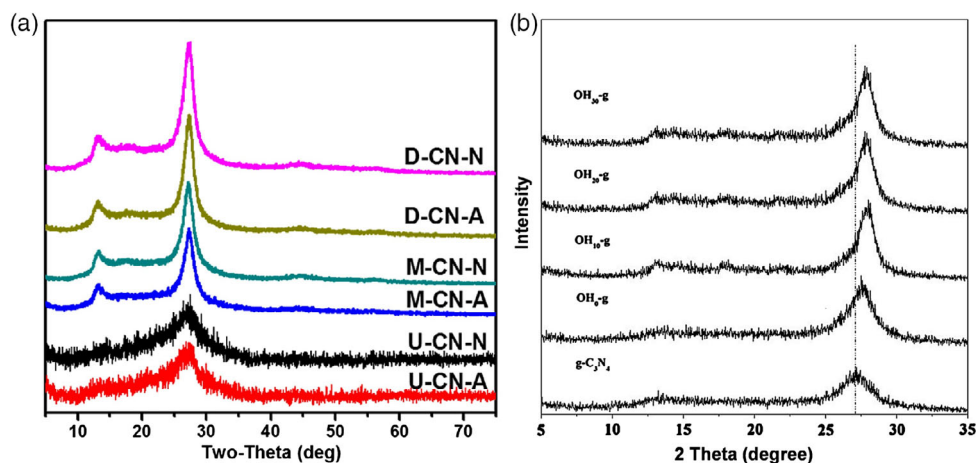


Figure 4. a) XRD patterns of the prepared $g\text{-C}_3\text{N}_4$ samples which are denoted X-CN-Y, the X presents the precursor material used (D: DCDA; M: melamine; U: urea) and Y presents the applied reaction conditions (A: air and N: nitrogen gas), b) XRD spectrum of $g\text{-C}_3\text{N}_4$ and hydroxylation modified samples with 0, 10, 20, and 30 wt% concentration H_2O_2 , respectively. a) Adapted with permission.^[37] Copyright 2017, Elsevier. b) Adapted with permission.^[38] Copyright 2016, Elsevier.

the consistency of the results would improve their accuracy. The effect of thermal treatment on the structure can be observed using the Raman spectra, XRD patterns, SEM and transmission electron microscopy (TEM) images of $g\text{-C}_3\text{N}_4$.

The in situ characterization methods are essential to analyze the growth mechanism of the $g\text{-C}_3\text{N}_4$ as it is difficult to control the final product. Various in situ characterization techniques, such as in situ heating TEM^[43] and thermogravimetric analysis coupled with Fourier-transform infrared spectroscopy (FTIR)^[44], can be used to investigate the calcination of supramolecular precursors. Also, structural characterization as well as direct imaging after calcination can be carried out via in situ heating SEM measurement.^[45] In addition, developing in-depth characterization approaches for highly active single-atom catalysts to understand the dynamic evolution during catalytic reactions at the atomic level is so important.^[46] In a recent study by Zhang et al.,^[47] charge transfer, changes in oxidation states, and dynamic evolution of chemical bond was observed via in situ characterization in single-atom Pt- C_3N_4 catalysts used for the photocatalytic splitting of water. By utilizing synchronous illumination X-ray photoelectron spectroscopy (SI-XPS), it was reported that the cleavage of Pt-N bond led to the formation of a Pt^0 species and the subsequent rearrangement of C-N into C=N, when excited under light. Moreover, SEM, high-resolution transmission electron microscopy, and elemental mapping of S-Pt- C_3N_4 revealed the structure and distribution of Pt on C_3N_4 nanorods. Techniques such as high-angle annular dark-field scanning transmission electron microscopy and X-ray absorption fine structure spectroscopy was also applied for in-depth examination of structural and coordination properties. In situ X-ray absorption spectroscopy is a handy technique used to characterize the vacant states and structural properties of excited atoms as well as to examine the transformation in catalysts. It can also be coupled with other tools to investigate local structural behavior in C_3N_4 -based nanomaterials.^[48]

To analyze the conductivity of C_3N_4 -based materials, two contact methods can be used. Two contact method has been applied

to perform conductivity comparison of C_3N_4 -based materials synthesized at various temperatures^[49] and having different shapes.^[50] The electronic conductivity is calculated using Ohm's Law. Furthermore, electron paramagnetic resonance (EPR) or electron spin resonance (ESR) spectroscopy has also emerged as a highly sophisticated and nondestructive tool for the detection of free radicals, metallic ions, defects, photoelectrons, and conjugated structure. This characterization technique has been readily used to confirm the presence of vacancies in the structure^[51] and to inspect the electronic band structure of $g\text{-C}_3\text{N}_4$.^[52] Shen et al.^[53] showed the use of ESR to confirm the enrichment of $g\text{-C}_3\text{N}_4$ with carbon vacancies. A strong ESR signal corresponds to a greater number of unpaired electrons, which can be attributed to the C defects in $g\text{-C}_3\text{N}_4$, which led to a reduced exciton-effect and enhanced production of charge carriers. Moreover, in a recent study by Xia et al.,^[54] EPR technique was applied to analyze the hybrid structure and π -conjugated structure of tri-s-triazine unit of $g\text{-C}_3\text{N}_4$ under illuminated and dark conditions. As photocatalytic activity of $g\text{-C}_3\text{N}_4$ is related to the formation of π -conjugated structure, EPR provided invaluable information. Under light conditions, electron transfer takes place from σ -type bonds to the π -conjugated structure, hence photoelectrons are produced. Moreover, using this technique, the hydroxyl radicals ($\cdot\text{OH}$) and superoxide radicals ($\cdot\text{O}_2^-$) were observed during the photocatalysis of $g\text{-C}_3\text{N}_4$. Using the proposed EPR-based method, the concentration of photoelectrons in $g\text{-C}_3\text{N}_4$ under light can be investigated, which would in turn aid in understanding the photocatalytic performance of $g\text{-C}_3\text{N}_4$ in hydrogen production. Zhao et al.^[55] utilized a system which coupled highly rapid spectroscopy with in situ ESR to study the dynamic changes in charge and energy transfer in 2D CNNSs. This technique helped in direct detection of photoelectrons and holes in the produced supramolecular complexes. A higher ESR signal indicated that π -electrons were redistributed in the complex framework or the π -conjugated system experienced extended delocalization.

4. Surface Functionalization of g-C₃N₄

Surface functionalization of graphitic materials is a versatile method to create active anchoring sites and to tune the chemical and electronic properties of the material. So far, many strategies have been used to prepare carbon-based advanced functional materials successfully.^[56] These strategies can be divided into two main types, namely, covalent, and noncovalent. The covalent strategies can cause permanent modifications and require well-controlled chemistries. They usually create defects by damaging the sp² framework of the material in subject, which has considerable effect on the electrical properties. However, these defects can be highly useful in many applications (e.g., catalysis, composites), if the defect density is tuned carefully. On the other hand, noncovalent strategies have simpler application processes but no adverse effect on the original structure. In this section, the adaptation of covalent and noncovalent strategies for the surface functionalization of the g-C₃N₄ are discussed extensively.

4.1. Covalent Strategies for Surface Functionalization

4.1.1. Reductions

The framework of g-C₃N₄ is mainly composed of sp²-hybridized carbon and nitrogen atoms, which modulates electronic properties as well as the surface chemistry. Graphite-like structure of g-C₃N₄ opens up the way for the use of reductive chemistries previously carried out on the other sp²-hybridized carbon nanomaterials.^[56b] Among the known chemistries, the framework charging appears as one of the best reduction approach due to

its tunability and it was shown to be effective on CNTs^[57] and graphene.^[58] This approach uses a one-pot reaction through the use of sodium naphthalide (NaNp) in suitable solvents (e.g., *N,N*-dimethylacetamide [DMAc], THF) allowing direct synthesis of negatively charged carbon nanomaterials. Recently, the framework charging method has been shown to be effective for the exfoliation and functionalization of polytriazine imide (PTI).^[59] In this study, highly reactive NaNp dissolved in DMAc reacted with the g-C₃N₄, and desired exfoliation of negatively charged PTI was accomplished by the framework charging (Figure 5a). The generated negative charges were further utilized to add surface functionalities such as long alkyl chain on the PTI. In principle, this method offers a tunability over the degree of negative charges as well as the functional groups created on the g-C₃N₄ surface, and thus it may be used for the fine-tuning of chemical and electronic properties of the g-C₃N₄ before target applications. The study found the optimum PTI/Na ratio for the best exfoliation of PTI as 7:1, although the fine-tuning of the charge density was also shown (Figure 5b). The color change of the PTI dissolution was evident for the alteration of the electronic properties. Moreover, exceptional stability and a 35 wt% yield was reported for 2D few-layered PTI (FL-PTI) solutions when the PTI/Na ratio of 7:1 was used (Figure 5c).

The simultaneous exfoliation and modification of g-C₃N₄ via reductive alkylation was also demonstrated in anhydrous THF. In contrast to the aforementioned method, g-C₃N₄ was reduced by lithium in the presence of naphthalene.^[60] The dodecyl functionalized g-C₃N₄ had a reduced bandgap which enhanced the

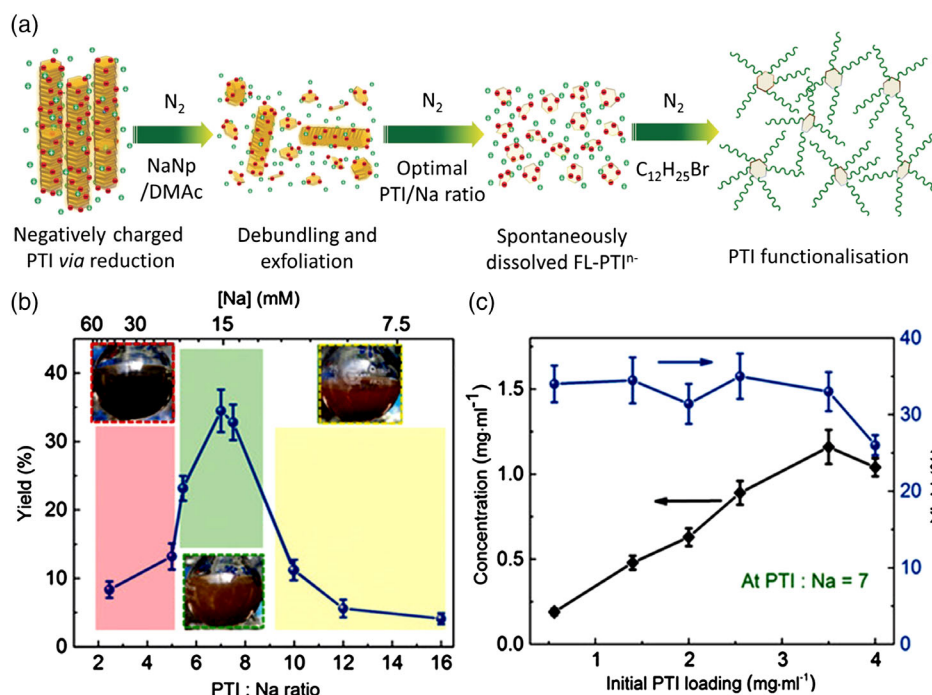


Figure 5. a) The schematic for surface charging and exfoliation of PTI. b) The effect of PTI/Na ratio on the degree of exfoliation and the electronic properties of PTI dissolution. Yellow, green, and red rectangles correspond to low-to-high [Na], respectively, with the inset photographs showing resultant negatively charged PTI dissolution. c) Effect of the initial PTI amount on the concentration/yield of negatively charged PTI dissolution (7:1 PTI/Na ratio). Adapted with permission.^[59] Copyright 2018, Wiley-VCH GmbH.

photoresponse and the visible-light harvesting ability, suggestive of more charge carriers generated under visible-light irradiation.

4.1.2. Oxidations

Oxidation can be effectively used to prepare highly stable suspensions of carbon nanomaterials under highly oxidizing conditions. This results in the insertion oxygen functional groups on the g-C₃N₄ surface. Even though the g-C₃N₄ exhibits considerable resistance against acids and bases (e.g., HCl, NaOH), strong oxidants (e.g., H₂SO₄, KMnO₄, and H₂O₂) can provide the chemical oxidation of g-C₃N₄ to form highly dispersible, surface-functionalized C₃N₄-based materials. Oxidation of the carbon nitride using H₂SO₄/KMnO₄ was shown to produce polar functional groups, such as amine, carboxyl, and ketone groups, on the surface. Functionalized material, which was used in a cell-imaging study by confocal fluorescence microscopy, showed enhanced dispersibility in water without surfactants or stabilizers.^[61] The pristine g-C₃N₄ was thermally oxidized by heating in pure oxygen atmosphere at varying temperatures and heating periods.^[62] As a result, the specific surface area increased, the light absorption range became broader, and separation of photogenerated charge carriers accelerated. Also, this modification boosted the photocatalytic hydrogen production by 4.3 times compared with the pristine one. In another study, oxidation of the g-C₃N₄ using H₂O₂ was found to be effective to create oxygen-containing functional groups on the surface and the functionalized material showed enhanced activity for rhodamine B degradation.^[38] In addition to the use of strong oxidizers to create oxygen-containing moieties on the g-C₃N₄ surface, a bottom-up approach which uses a novel nitrogen-rich precursor bearing hydrochloride groups, so-called semicarbazide hydrochloride (ONLH), was shown to increase the amount of oxidized content in the structure of g-C₃N₄.^[63] The oxygen concentration was controlled thermally by carrying out the synthesis at different temperatures.

4.1.3. Cycloadditions

Cycloadditions are one of the most versatile routes to the covalent chemical modification of sp²-hybridized carbon nanomaterials such as CNTs^[64] and graphene.^[65] Similar to the CNT chemistry,

the surface of g-C₃N₄ polymer was modified using the 1,3-dipolar cycloaddition of in situ generated azomethine ylides prepared by thermal condensation of the α-amino acid *N*-methylglycine and an aldehyde (Figure 6).^[66] The surface-modified g-C₃N₄ polymers with diverse organic groups, including aryl, aryl acid, pyridine, ionic liquids, and ferrocene showed varying electronic properties compared with the pristine g-C₃N₄ and were used as catalyst for the selective oxidation of 3,5,5-trimethylcyclohex-3-en-1-one using atmospheric oxygen.

A ball-milling assisted solid-state mechanochemical method, which exfoliated the g-C₃N₄ and generated the reactive radicals and ions on the surface of g-C₃N₄, was used to covalently graft fullerene (C₆₀) on the edge planes of the g-C₃N₄ in the presence of lithium hydroxide (LiOH).^[67] Spectroscopic characterizations (e.g., Raman and XPS) revealed the covalent bonding of C₆₀ onto the edges of CNNSs via a four-membered ring of azetidine.

4.1.4. Cross-Coupling Reactions

Covalent functionalization of carbon nitride frameworks through cross-coupling reactions were studied using a carbon nitride framework with a halogen (Cl, Br, and I)-substituted phenyl (Figure 7).^[68] In a cross-coupling reaction, the halogenated phenyl-group-modified carbon nitrides were subjected to a reaction with a phenylboronic acid and a *tert*-butyl acrylate through Suzuki and reductive-Heck cross-coupling reactions, respectively. The final covalently modified carbon nitrides displayed enhanced dispersibility in many solvents, such as dimethyl sulfoxide, THF, *n*-hexane, and diethyl ether, suggestive of surface group addition. The potential photocatalytic activity of the prepared catalysts was tested by the efficient photo-oxidation of benzyl alcohol as a model reaction in an organic solvent and they showed enhanced photocatalytic activity compared with the unmodified carbon nitrides.

4.1.5. Copolymerizations

Copolymerization can be described as a molecular doping method used for the modification of traditional π conjugation systems, and their optical absorption, electronic band structure and properties, and photocatalytic behavior.^[12b] Combining

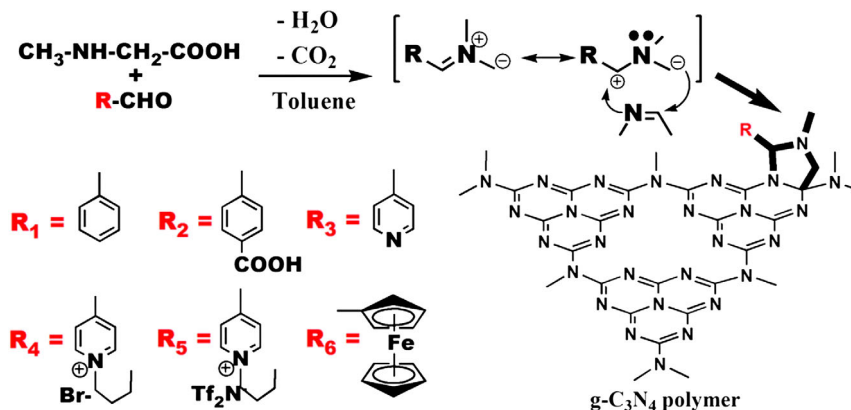


Figure 6. The 1,3-dipolar cycloaddition reaction of azomethine ylides with the pristine g-C₃N₄. Adapted with permission.^[66] Copyright 2014, the Royal Society of Chemistry.

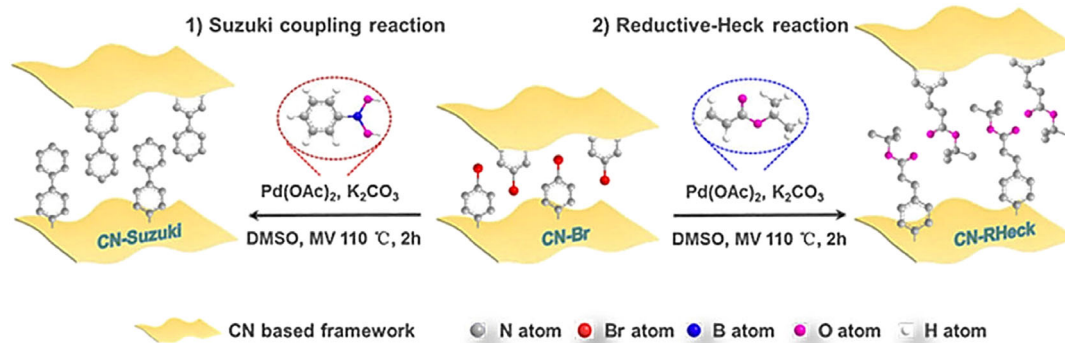


Figure 7. The schematic for the postcovalent functionalization of CN-Ph-Br via Suzuki and reductive-Heck reaction. Adapted with permission.^[68] Copyright 2018, Wiley-VCH GmbH.

$g\text{-C}_3\text{N}_4$ with polymers leads to more advanced functionalities. In addition, the photoinitiation, photocatalysis, or photoluminescence properties of $g\text{-C}_3\text{N}_4$ have been effectively developed and optimized in polymer hybrids, due to enhanced delamination and synergy between the materials. Polymer-modified $g\text{-C}_3\text{N}_4$ and their applications are shown in Table 2.^[69] Fan et al. reported usage of terephthalaldehyde as an inexpensive aromatic comonomer to create aromatics-grafted $g\text{-C}_3\text{N}_4$ -based copolymer with better electrical conductivity and charge separation performance for hydrogen production.^[70] With this strategy, most of the aromatics can be grafted into the network of C_3N_4 . Adding an optimized quantity of polymer to the precursor of C_3N_4 during the synthetic process is one of the most cost-effective copolymerization methods. In biosensor applications, better sensitivity and selectivity are offered by polymer-functionalized $g\text{-C}_3\text{N}_4$ due to dispersion enhancement and the sensing site's access. The polymeric matrix doped with $g\text{-C}_3\text{N}_4$ not only improves the efficiency of the electrode materials used for energy storage application but also makes them more stable in comparison with the pure polymer matrix. Also, $g\text{-C}_3\text{N}_4$ can serve as an effective photoinitiator during the synthesis of polymer particles. Better dispersibility and processability of polymer-modified $g\text{-C}_3\text{N}_4$ can also be useful for thin-film formation.^[71]

Supramolecular preorganization of $g\text{-C}_3\text{N}_4$ is one of the important methods to functionalize and tune $g\text{-C}_3\text{N}_4$. Significant parameters that influence the structure of the product are: sequence of the monomer, type of the solvent, and reaction times.^[72] Zhou et al.^[73] produced supramolecular C_3N_4 nanocomposite using melamine-cyanuric acid and barbituric acid as monomers. The surface area so obtained was superior to that of pure $g\text{-C}_3\text{N}_4$. Moreover, to regulate heteroatom doping and

tune structure of $g\text{-C}_3\text{N}_4$, a supramolecular precursor self-assembly method was developed by Wang et al.^[74] In addition, the density functional theory (DFT) simulations in this study, provides a unique model for $g\text{-C}_3\text{N}_4$ functionalization. In another study, phosphorus-doped hexagonal tubular $g\text{-C}_3\text{N}_4$ was obtained by applying the phosphorous acid-assisted hydrothermal method and thermal treatment, respectively.^[75] Consequently, a large surface area was achieved, which enabled the number of reactive sites to increase.

4.1.6. Miscellaneous Covalent Surface Functionalizations of $g\text{-C}_3\text{N}_4$

On the structure of the $g\text{-C}_3\text{N}_4$, there are free NH_2 groups and these primary amine groups are highly reactive to many reagents including anhydrides, acyl halides, aldehydes, and carboxylic acids. The electronic structure of carbon nitride was modified by introducing imide functional groups on its framework through amidation reaction between free NH_2 groups and pyromellitic dianhydride.^[76] The resultant new polymeric photocatalyst responded to visible-light and showed enhanced photocatalytic methyl orange degradation, attributed to the separation of the photoinduced electrons and holes. In another example, CNTs were covalently bound to the $g\text{-C}_3\text{N}_4$ surface.^[77] In this covalent addition, CNTs were initially oxidized to produce carboxylic acid groups on the surface and these groups were chlorinated using SOCl_2 to yield acyl chloride group on the nanotube surface. The reaction between free NH_2 groups on the $g\text{-C}_3\text{N}_4$ and the acyl chloride groups on CNTs yielded CNT-functionalized $g\text{-C}_3\text{N}_4$. The obtained covalently bonded hybrid photocatalyst showed enhanced activity for O_2 reduction reaction to H_2O_2 in presence of formic acid. Observed activity

Table 2. Polymer modified $g\text{-C}_3\text{N}_4$ and their applications.

Application area	Composition	Synthesis methods	Enhanced properties	Ref.
Electrochemiluminescence biosensor	PPy/ $g\text{-C}_3\text{N}_4$	In situ polymerization	Improved electroconductive network, high sensitivity	[69a]
CO_2 reduction	1 H,1 H,2 H,2 H-perfluorodecanethiol/ PGMA/ $g\text{-C}_3\text{N}_4$	Photoinduced chemical reaction	Improved mass transfer of CO_2 by 34 times	[69b]
Supercapacitors	Camphor sulfonic acid/polycarbazole/ $g\text{-C}_3\text{N}_4$	Chemical oxidative polymerization	Improved charge transfer and structure stability (over 1000 cycles)	[69c]

was attributed to enhancement of the photoinduced electron generation. Similarly, another amidation reaction between zinc tetracarboxyphthalocyanine (ZnTcPc) and $g\text{-C}_3\text{N}_4$ yielded the covalently functionalized $g\text{-C}_3\text{N}_4\text{-ZnTcPc}$ ($g\text{-C}_3\text{N}_4/\text{ZnTcPc}$) hybrid photocatalyst.^[78] Efficient electron transfer from the lowest unoccupied molecular orbital of ZnTcPc to the conduction band of $g\text{-C}_3\text{N}_4$ mitigated the charge recombination probability and enhanced the photocatalytic activity for the degradation of rhodamine B and 4-chlorophenol under visible irradiation.

In a recent study, Windle and coworkers synthesized a novel photocatalyst for hydrogen production, which involved the covalent attachment of nickel bis-amino thiophenol catalyst onto four types of 2D $g\text{-C}_3\text{N}_4$, including three of them prepared from urea, DCDA, and ONLH, and an oxygen-doped one produced by treating the DCDA-based C_3N_4 with formic acid (FAT). These CN-catalyst hybrid materials, namely $\text{CN}_{\text{urea}}\text{-Ni}(\text{abt})_2$, $\text{CN}_{\text{DCDA}}\text{-Ni}(\text{abt})_2$, $\text{FAT-Ni}(\text{abt})_2$, and $\text{ONLH-Ni}(\text{abt})_2$, were formed as a result of the coupling of aryl amines and aryl chlorides in the presence of potassium *tert*-butoxide catalyst (Figure 8).^[79] The CN-catalyst materials exhibited over 8 days of hydrogen evolution, rapid and lasting charge separation, and photoactivity under irradiation of 475 nm light. Although the surface area was found to be related to catalyst loading, the lowest loading was observed for CN_{DCDA} that had a surface area higher than FAT. This confirms that the chemical composition of the surface also played a role in defining the loading capacity. CN_{urea} was the most efficient due to its impressively high quantum yield. Moreover, the oxygen-doped CNs can utilize a broader region of the visible spectrum than the nondoped ones. On the other hand, CN_{urea} and CN_{DCDA} were the only materials to undergo substantial reduction for electron transmission to $\text{Ni}(\text{abt})_2$ as well as $\text{Ni}(\text{bdt})_2$; however, this transfer was higher for the former catalyst than the later one and this affected their respective hydrogen production capability.

4.1.7. Photoinduced Functionalization of $g\text{-C}_3\text{N}_4$

Photoinduced functionalization is lately used as a method to obtain better dispersibility especially producing the preferable $g\text{-C}_3\text{N}_4$ thin films. Cao et al. present a unique polymer $g\text{-C}_3\text{N}_4$ combining method as polymer-grafted $g\text{-C}_3\text{N}_4$.^[80] Methyl methacrylate, glycidyl methacrylate, and isobornyl acrylate

polymerized separately by adding $\text{Cu}(\text{I})\text{Br}$, ligand, and initiator at 45 C for 30 min. Using graft polymer brushes these polymers grafted on a $g\text{-C}_3\text{N}_4$ surface. The poor dispersibility of $g\text{-C}_3\text{N}_4$ in organic solvents is one of the challenges to produce thin films. However, the polymer/ $g\text{-C}_3\text{N}_4$ structure enhanced dispersibility and enable smooth surface spin coating.

Sheng et al.^[81] used surface-initiated photo grafting and photopolymerization (SIPGP) technique for producing polymer brushes which are polystyrene (PS), poly(methylmethacrylate), poly(*N,N*-dimethylaminoethyl methacrylate), poly(*N*-isopropylacrylamide), poly(3-sulfopropyl methacrylate), and poly(2-(methacryloyloxy)ethyl trimethylammonium chloride) on the $g\text{-C}_3\text{N}_4$ surface. After SIPGP the samples were washed with proper solvent considering monomer type. Moreover, spin-coated and microcontact printed $g\text{-C}_3\text{N}_4$ also graft polymer brushes and characterized. It is confirmed that the physical characteristics of surface-functionalized $g\text{-C}_3\text{N}_4$ remained as $g\text{-C}_3\text{N}_4$ by UV-vis absorption spectroscopy. This promotes chemical/biosensor applications of functionalized $g\text{-C}_3\text{N}_4$.

In another study, cyanuric acid-melamine hydroxyl ethyl methacrylate (CM-HEMA) precursor which has good dispersibility, was synthesized using visible-light irradiation. Heat treatment curing provides a gentle surface and stable thermoset coating. CM-HEMA films modified with poly-(styrene) and poly(*N,N*-dimethylacrylamide), so the tuned surface features and selectivity enabled the applications such as photocatalytic and photoelectrode. Both FTIR and elemental analysis were used for identifying grafting.^[82]

4.2. Noncovalent Strategies

Noncovalent modifications include van der Waals forces, p-p interaction, hydrophobic interaction, electrostatic attraction, and hydrogen bonding. Such noncovalent strategies are mainly involved in noncovalent interaction of small organic molecules and nanoparticles.

4.2.1. Noncovalent Interaction of Organic Molecules

One of the methods for enhancing the electronic and optical properties of C_3N_4 is the physical adsorption of organic

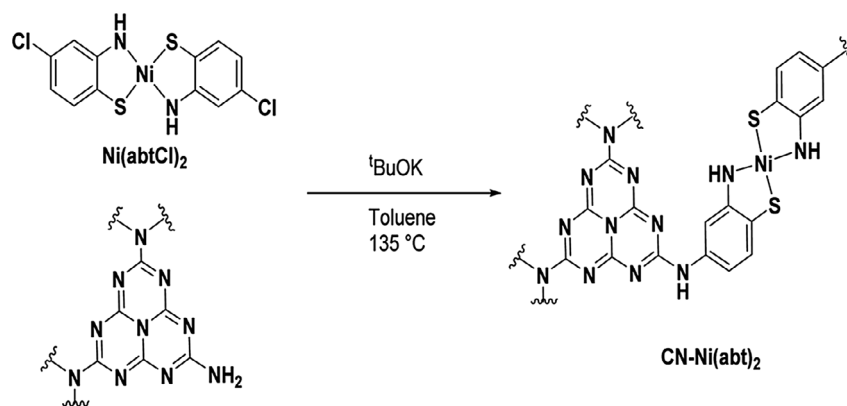


Figure 8. Covalent addition of molecular catalysts on $g\text{-C}_3\text{N}_4$. Reproduced under the terms of the Creative Commons Attribution 3.0 Unported Licence.^[79] Copyright 2020, the Authors. Published by the Royal Society of Chemistry.

molecules on g-C₃N₄ surface. The redox band edge positions may be modified with the organic molecules on the surface of the C₃N₄. The DFT is one of the computational quantum mechanical modeling methods that are used to reveal the characteristics of the valence and conduction bands, the effective mass of carriers, band edge positions, and optical properties. Accuracy of DFT depends on whether the simulated crystal is a good approximation of reality or not, and various other factors, including the material type and studied property. Zhang et al.^[83] proposed a theoretical model that shows photocatalytic activity enhancement of small organic molecule absorbed g-C₃N₄. They modified g-C₃N₄ photocatalyst with different heterocyclic small molecules as a ligand (thiophene, furan, pyrrole, or pyrrol) and investigated the properties of modified g-C₃N₄, including their electronic structure, effective carrier mass, position of band edge, and optical properties, by DFT calculations. Considering the fast transfer of electrons in the pyrrole-modified g-C₃N₄, it was acknowledged to be a praiseworthy photocatalyst. A study on the noncovalent interaction between the 2,4-dinitrophenylhydrazine (2,4-graphitic DNP) derivatives and carbon nitride was also conducted.^[84] Derivatives of 2,4-DNP hydrazine were produced and combined with g-C₃N₄ to increase the light absorption of the resulted photocatalyst. Some of the spectroscopic techniques, such as the FTIR and UV-vis, were used for characterization in different polar solvents like *N,N*-dimethylformamide (DMF) and acetonitrile (ACN). Doping g-C₃N₄ with 5% of dinitrophenylhydrazine derivatives led to absorption in the visible region and facile charge immobilization, which indicates reduced optical bandgap. Experimental results were found to be in line with DFT.

4.2.2. Noncovalent Interaction of Nanoparticles

Preparation of semiconductor-noble metal composites can enhance photocatalytic efficiency as well as photogenerated electron-hole separation. Noble metals with localized surface plasmon resonance (SPR) demonstrate strong absorption of visible light. In addition, the adsorption efficiency of the C₃N₄ improves due to the existence of metal nanoparticles. Qin et al. increased the visible-light absorption, by the decoration of g-C₃N₄ surface by Ag nanoparticles via chemical reduction.^[85] The improvement in visible-light absorption of Ag-deposited g-C₃N₄ was supported by the localized SPR effect, which caused a reduction in photogenerated electron-hole generation and improved photocatalytic performance. The photocatalytic activity development is primarily dependent upon both the synergistic effect between the components and the proper load amount of Ag. The 3 wt% Ag-loaded Ag/g-C₃N₄ composite offered the best photoactivity, which was about 3.6 times higher than that of pure g-C₃N₄. Yuan et al. produced ZIF-8/g-C₃N₄ composites via the ultrasonic in situ method.^[86] Visible-light absorption, electron transfer, and the photocatalytic reaction rate are improved due to the unique hybrid structure. Upgraded photocatalytic performance and excellent stability were observed in ZIF-8/g-C₃N₄ composites.

In another assay, Wang et al.^[87] revealed the distinctive hole-accepting feature of microwave-synthesized carbon dot (^mCD) using transient absorption spectroscopy (TAS). The ^mCD/CN composite supports electron accumulation on the surface of

CN as a result of hole transfer to ^mCD. It was also observed that sonication-based carbon dot (^sCD) serves as an electron acceptor in ^sCD/CN, whereas ^mCD acts as a distinguished hole acceptor in ^mCD/CN after excitation.

4.3. Surface Functionalization via Elemental Doping

Doping, the process of addition of structural impurities, has been known as an efficient method to change the bandgap and band structures of g-C₃N₄. It also expands the light absorption and increases the separation of the electron-hole pairs. In elemental doping, impurities can be metallic or nonmetallic. The effect of doping with metalloid group elements was also reported in a recent study.^[88] Doping with anions is reported to result in hybridization of p-orbitals of the dopants with those of g-C₃N₄, whereas cation doping produces a discrete band through 3d orbitals of transition metals leading to fine-tuning of the valence band. However, when codoped, anions and cations aids in bandgap adjustment as well as keeps the balance within charges.^[89]

4.3.1. Metallic Doping

Metallic impurities are commonly incorporated into the g-C₃N₄ structure using a homogenous solution of g-C₃N₄ precursor and metallic salt. This mixture when subjected to thermal condensation produces g-C₃N₄ decorated with metallic ions.^[11] Generally, elements from the lithium family (K⁺, Na⁺) and transition metals (Pt, Pd) are used. But in recent years, this method has also been utilized for other transition metals, such as Cu, W, and Mo.^[90]

The overall effect of K and Na doping on g-C₃N₄ is quite similar; however, K-doped materials perform better in photocatalytic applications.^[91] On the other hand, noble metal doping boosts movement of carrier, improves electron-hole separation, and narrows the bandgap. Transition metals, including Fe, Cu, W, Zn, Mo, and Zr, have mainly gained the attention of researchers as doping elements.^[11]

The work by Das et al.^[92] highlighted the role of cobalt (Co) doping on the photoluminescence characteristics, the photocatalytic activity, and stability of the g-C₃N₄ structure. The doped material demonstrated an increased surface area, decreased PL intensity, better stability, and better photocatalytic behavior under light than the pristine g-C₃N₄. Electrons were trapped due to the addition of Co and this helped in separation of carriers of charge.

Doping of g-C₃N₄ with S-block elements, such as lithium, sodium, potassium, magnesium, calcium, strontium, and barium, was investigated by Fronczak et al.^[93] Cyanamide was chosen as the precursor while corresponding metal chloride was used to produce the samples via polycondensation. The elemental doping was found to have positive effects on the surface, texture, morphology, as well as structural characteristics of g-C₃N₄. S-block dopants promoted the adsorption of g-C₃N₄, which triggered the elimination of methyl blue and copper ions from aqueous media.

While metals promote the electron–hole separation, high cost, defects found in them, and poor thermal stability of ions are some limitations.^[11,88]

4.3.2. Nonmetallic Doping

Nonmetals have high ionization energy and electronegativity and can form a covalent bond by reacting with other components. Nonmetallic doping facilitates in tuning the absorbance, redox potentials, and movement of photoinduced charge carriers.^[11] Different nonmetallic dopants such as phosphorus,^[94] sulfur,^[95] carbon,^[96] nitrogen,^[97] oxygen,^[98] boron,^[99] and halogens (e.g., fluorine^[100] and iodine^[101]) have been used. Elements with low electronegativity, such as F, B, S, and P, narrow down the bandgap.^[88] Oxygen doping boosts adsorption ability, promotes the production of photogenerated holes, increases the surface area, and improves the separation of photogenerated charge carriers.^[11]

The theoretical study by Ghashghaee et al. reported the effect of B, O, S, and P doping on the siting and electronic characteristics of triazine and heptazine structures of g-C₃N₄.^[102] O and S preferred to substitute bridging N atoms, whereas B occupied the places of internal carbon atoms in the bigger rings at the center. P replaced bridging and interstitial two-coordinated N atoms in heptazine and triazine structures, respectively. Moreover, in contrast to the O, S, and P doping, B doping was driven by negative charges.

Tian et al. reported the fabrication of 3D ultrathin porous N-doped g-C₃N₄ from melamine using a simple hydrothermal pretreatment method along with calcination.^[103] Hydrothermal pretreatment makes urea a richer nitrogen source and porogen. N-doping refines the electronic structure of g-C₃N₄ and prevents the problem of incoming foreign atoms. This is one of the most impressive surface functionalization techniques to enhance the response of visible-light and photocatalytic activity of g-C₃N₄.^[103] Bai et al. proposed a one-step modification scheme to produce highly porous, S-doped g-C₃N₄.^[104] The impressive enhancement in the photocatalytic behavior of the doped material was attributed to the synergy between high porosity and doped structure.

4.3.3. Codoping

Codoping conveys the individual benefits of each of the dopants and enhances the structural and optical properties of g-C₃N₄. K–Na,^[105] Cu–Fe,^[106] P–O,^[107] and S–P^[108] are some of the significant doping combinations. Regarding the effect of codoping, K–Na doping enlarges the surface area and enhances the rate of separation in photogenerated charges. Babu et al. studied the effect of bielemental doping, i.e., with B and S on g-C₃N₄.^[109] The g-C₃N₄ decorated with B and S showed improved absorption of light, superior separation of charges, better electron transfer, and greater effective surface area than undoped or singly doped materials. Moreover, codoping caused defects in which photoelectrons were stuck and photogenerated charge carrier could not recombine.

Dou et al. codoped g-C₃N₄ with metallic Fe(II) and nonmetallic S.^[89] The mixture of melamine and ferrous chloride in

trithiocyanuric acid was used to synthesize the codoped product, which demonstrated excellent photodegradation for RhB under illumination. According to the theoretical estimations by DFT, codoping effectively reduced the bandgap and provided more active sites, which in turn enhanced electron–hole transfer. Yang et al.^[110] also reached a similar conclusion by synthesizing a nitrogen-deficient g-C₃N₄ with melamine and doping it with ammonium phosphate and ammonium chloride. The structure codoped with P and Cl showed a more negative conduction band potential. For more insight into the effect of different dopants on the structure and properties of g-C₃N₄, readers are directed toward the review by Jiang et al.^[111]

The aforementioned surface modification techniques improve the electronic properties of the surface and accelerate photocarrier separation. Moreover, polymer-modified g-C₃N₄ benefits from enhanced dispersibility and processability, which makes it suitable for film formation. Using the most suitable surface modification for a particular application is of great significance. Elemental doping is very useful for tuning the bandgap of semiconductive g-C₃N₄. In a nutshell, K–N, O, N, and C–Fe doping result in larger surface area, better absorption ability, a modified electronic structure, and reduced bandgap, respectively.

5. Processing of C₃N₄

Processing of C₃N₄ leads to better mechanical properties, rapid hydrogen evolution under visible light, and suppressed recombination of photogenerated charges. It is mainly classified into C₃N₄-based structures and their hybrids with other nanomaterials. Due to the combination of favorable properties of both materials, C₃N₄ hybrid structure performs comparatively well. In this part, the C₃N₄-based thin films and hierarchical structures, C₃N₄-CNTs, and C₃N₄-graphene hybrid structures are discussed.

5.1. C₃N₄-Based Thin Films

Primarily, there are two processing approaches for the preparation of C₃N₄-based thin films, namely: bottom-up and top-down. As a bottom-up route, in thermal vapor condensation,^[111] melamine was heated to 600 °C with heating rates of 3 °C min^{−1} for 3 h in a crucible placed in a muffle furnace (Figure 9a). The growth of highly uniform g-C₃N₄ films was observed on the fluorine-doped tin oxide (FTO) substrate placed on the top of the crucible. The resulting films exhibited photocurrent density as high as 0.12 mA cm^{−2} at the bias of 1.55 V (vs reversible hydrogen electrode) with Na₂S as the sacrificial reagent, attributed to the intimate contact between the film and the substrate, decreased charge transport, and charge transfer resistance. Liquid-based direct growth method^[112] used supramolecular complexes (e.g., a mixture of cyanuric acid and 2,4-diamino-6-phenyl-1,3,5-triazine [CMP]) liquifying before thermal condensation at high temperatures. Produced porous C₃N₄ films displayed open-circuit voltage of greater than 1 V when used as the electron acceptor in a polymer solar cell (Figure 9b). The doctor-blade method is also used for producing porous supramolecular films at a large scale. The precursor pastes can be deposited on a range of substrates, such as FTO, porous TiO₂, silicon wafer, and glass, and the film thickness can be easily adjusted.^[113] Microcontact

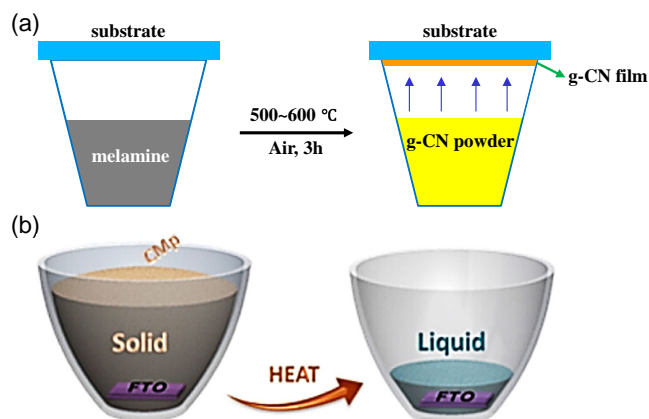


Figure 9. The deposition of $g\text{-C}_3\text{N}_4$ film via a) thermal vapor condensation and b) liquid-based direct growth. a) Adapted with permission.^[111] Copyright 2015, Elsevier. b) Adapted with permission.^[112] Copyright 2014, American Chemical Society.

printing^[114] appears as another approach that involves precursor (e.g., cyanamide) to be sandwiched between two substrates; the precursor gets condensed and printed on the substrates upon heating. To produce $g\text{-C}_3\text{N}_4$ on conductive substrates like carbon fiber, nickel foam, and FTO glass, electrophoretic deposition method is commonly used.^[115] The C_3N_4 -toluene suspension was prepared, and a direct current was applied between the conductive substrate and the counter electrode. This technique is especially useful for thermally unstable substrates.^[116] In addition, there are other bottom-up methods including solvothermal,^[117] sol-gel,^[118] and electrodeposition.^[119] On the other hand, in top-down processes, the films can be produced from the synthesized $g\text{-C}_3\text{N}_4$ following some traditional methods such as spraying^[120] and spin coating.^[121] The aforementioned processes have several advantages and disadvantages when compared with each other. Readers interested in comprehensive comparisons are directed to the review article on films of $g\text{-C}_3\text{N}_4$.^[33,116,122]

Very recently, an original sputtering method using radio frequency magnetron (RFM) was used for the stoichiometric growth of photoactive C_3N_4 thin films.^[123] This method utilizes $g\text{-C}_3\text{N}_4$ powder in the compact form to serve as the sputtering target. The thin-film deposition was carried out on different substrates, including borosilicate glass and TiO_2 nanotubular array, under two different plasma media, i.e., Ar and N_2 at various time durations. According to their findings, in comparison with N_2 , Ar plasma enabled faster production of thinner and more stoichiometric C_3N_4 films with a higher current density. The most suitable time duration for RFM sputtering at 100 W, with $g\text{-C}_3\text{N}_4$ as target and Ar as plasma was found to be 3 h.

5.2. C_3N_4 -Based Hierarchical Structures

Hydrogels are notable polymeric materials with a crosslinked hydrophilic structure. Due to their unique swelling properties and ability to retain shape, they perfectly imitate human tissue and find extensive use in biomedicine, tissue-engineering, drug-delivery, self-healing, and shape-memory materials. However, these materials are limited by their weak mechanical

properties. To improve their mechanical properties, hydrogels are reinforced with particles that dissipate stress and provides extra stabilization through repulsion between charged filler particles. Amidst these bulk soft materials, $g\text{-C}_3\text{N}_4$ acts as a praiseworthy photoinitiator, and reinforcer and $g\text{-C}_3\text{N}_4$ /hydrogel hybrids exhibit excellent mechanical properties.

When $g\text{-C}_3\text{N}_4$ is exposed to light, radical formation occurs on its surface in an aqueous solution due to its photoactive nature.^[124] The surface of $g\text{-C}_3\text{N}_4$ works as an initiation platform and $g\text{-C}_3\text{N}_4$ are covalently embedded into the gel network. No transfer of electrons or the presence of an external crosslinker is required. Hence, $g\text{-C}_3\text{N}_4$, a monomer, and crosslinking agents such as water-soluble acrylamide derivatives, can lead to rapid hydrogenation under visible light irradiation.

$g\text{-C}_3\text{N}_4$ can be used for hydrogel formation through covalent bonds, integrated into hydrogels in the form of supramolecular hydrogel formation, and/or processed into the scaffolds of the gels to induce improved mechanical properties. Furthermore, the diversity of $g\text{-C}_3\text{N}_4$ enables the synthesis of new and improved hydrogels with unique properties like ultralow friction, thermo responsiveness, super stretch ability, and simultaneous toughness and flexibility. Photopolymerization and reinforcement via $g\text{-C}_3\text{N}_4$ help develop gels with superior spatial control. Very recently, a comprehensive review article has reported the role of $g\text{-C}_3\text{N}_4$ in polymerization reactions and the properties of $g\text{-C}_3\text{N}_4$ /polymer composite structures.^[125]

As shown in Figure 10a, photocatalysis by semiconductors involves the generation of charges under light, which in turn reacts with O_2 or H_2O to form free radicals.^[126] While $g\text{-C}_3\text{N}_4$ itself does not form hydroxyl radicals, it reduces oxygen to superoxide radicals, and the polymerization is initiated (Figure 10b). Using bulky $g\text{-C}_3\text{N}_4$ might not form stable hydrogel with polyacrylamide (PAM) as the chains have weak interaction within them. Moreover, bulky $g\text{-C}_3\text{N}_4$ neither disperses well in water nor distributes evenly in hydrogels. A solution for this was proposed by Dong and coworkers, who designed a composite hydrogel using alkali-exfoliated CNNSs as a crosslinking agent, initiator, and reinforcer in PAM.^[126] They proposed a simple hydrogel fabrication method using photoinduced polymerization. The photoactive CNNS initiated polymerization of acrylamide monomers, and a 3D network was formed due to hydrogen bonds. As a result, a hydrogel was formed with CNNS dispersed in it, as shown in Figure 10c. The synthesized product demonstrated extraordinary UV absorption and visible transparency capabilities, making it ideal for UV radiation shielding, fluorescence labeling, and photocatalysis. The produced hydrogels are flexible, photostable, and have self-healing properties.

Another limitation of $g\text{-C}_3\text{N}_4$ -based hierarchical structures is their inadequate structural porosity and recombination of photo-generated charges. Thus, Huang and coworkers^[127] fabricated a unique cellulose-derived hierarchical $g\text{-C}_3\text{N}_4$ / TiO_2 -nanotube heterostructure. As shown in Figure 11, the surface sol-gel process was used to fabricate the $g\text{-C}_3\text{N}_4$ / TiO_2 -NT nanocomposite. The natural cellulose extracted from regular filter paper by layer-by-layer self-assembly is used as a structural template for TiO_2 nanotube. Cellulose nanofiber surface was coated with ten layers ultrathin TiO_2 thin films and calcined at 450°C . TiO_2 nanotubes together with urea were crushed, and a mixture was prepared, which was again calcined in a closed crucible to finally form a

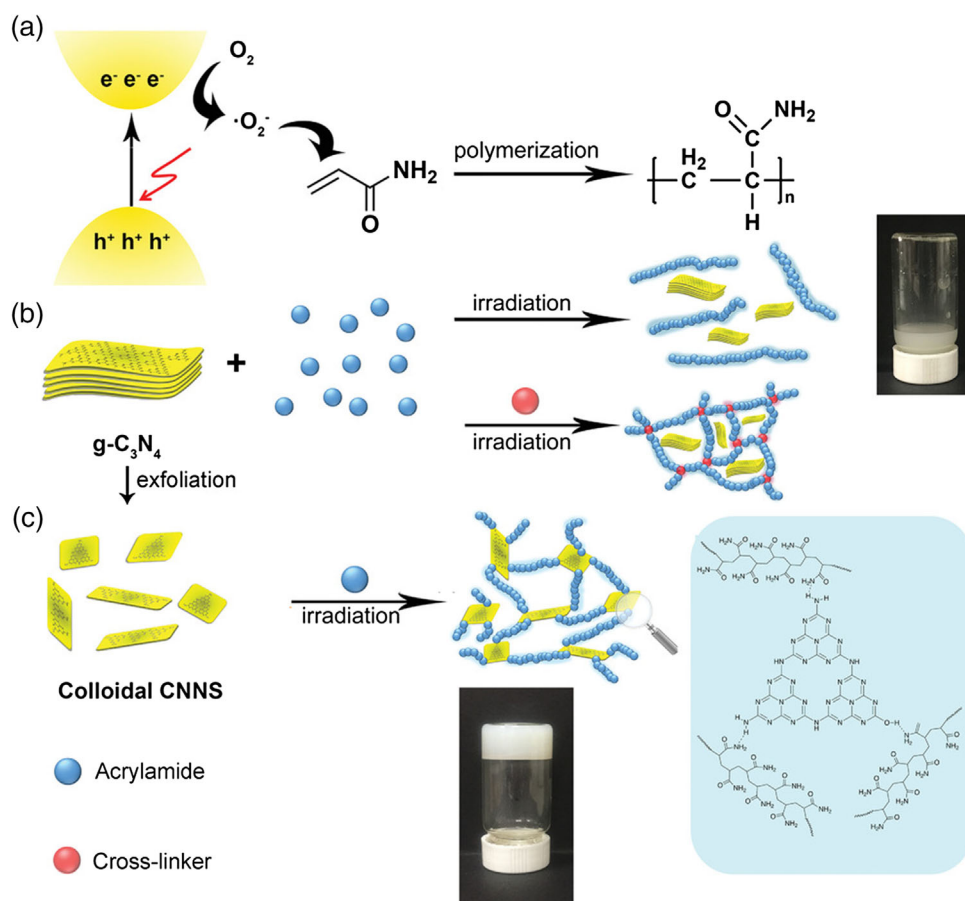


Figure 10. Illustration for the a) photoinitiated polymerization of acrylamide by $g\text{-C}_3\text{N}_4$ and the PAM gelation with b) $g\text{-C}_3\text{N}_4$, and c) CNNSs. Reproduced with permission.^[126] Copyright 2019, Wiley-VCH GmbH.

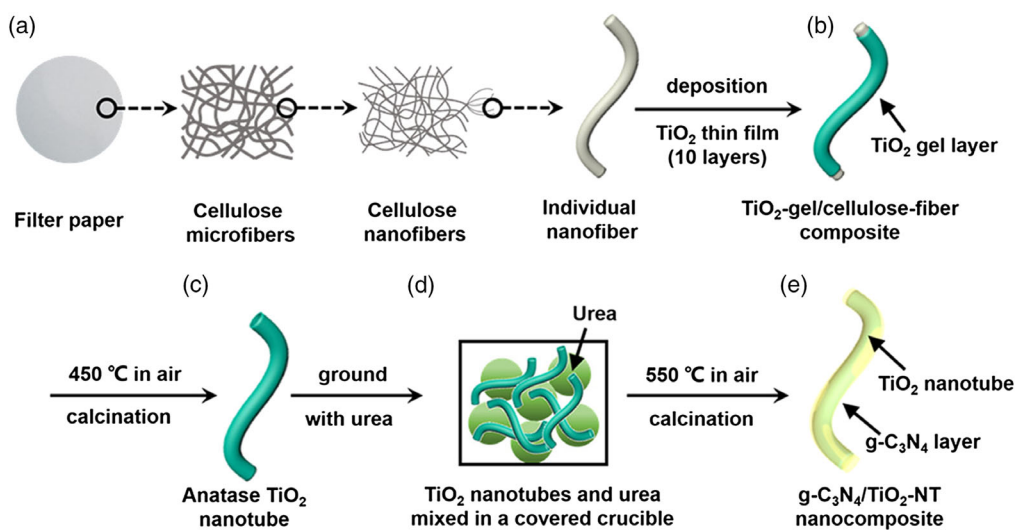


Figure 11. Schematic diagram showing the preparation process of the natural cellulose substance-derived $g\text{-C}_3\text{N}_4/\text{TiO}_2\text{-NT}$ nanocomposite. Reproduced with permission.^[127] Copyright 2020, American Chemical Society.

$g\text{-C}_3\text{N}_4/\text{TiO}_2\text{-NT}$ nanocomposite. The hierarchical network of the $g\text{-C}_3\text{N}_4/\text{TiO}_2$ composite was similar to that of cellulose, whereas close heterojunctions were observed within $g\text{-C}_3\text{N}_4$ and TiO_2 phases. As a result of this processing, the composite was found to have remarkable photocatalytic properties, superior transfer efficiencies of photogenerated charges, and a photoresponse range extending from UV to visible-light region of the spectrum.

5.3. $g\text{-C}_3\text{N}_4/\text{CNT}$ Hybrid Structures

$g\text{-C}_3\text{N}_4/\text{CNT}$ structures are traditionally produced either by physical mixing of the two or through in situ immobilization of $g\text{-C}_3\text{N}_4$ on CNTs. Both these methods are marred by limitations such as nonuniform mixing and insufficient contact and in some cases decrease in N content due to heat treatment at elevated temperatures. In addition, 2D CNNSs were produced by thermal oxidation etching followed by liquid exfoliation to enhance their interaction with other materials. While this technique faced yield-related problems, the interlayer distance between the layered $g\text{-C}_3\text{N}_4$ was opened up, leading to the enlarged surface area, enhanced physicochemical properties, and improvements in photoactivities.

A versatile method to self-assemble CNNSs and CNTs at low temperatures was shown to form $g\text{-C}_3\text{N}_4$ NS–CNT heterostructures.^[128] This method made use of the π – π stacking and electrostatic interactions. Three-dimensional hybrid structures made up of CNNSs and CNTs offered promising catalytic activity for oxygen evolution as well as stability. The $g\text{-C}_3\text{N}_4$ protonated with

hydrochloric acid to decrease the exfoliation time and provide a homogeneous distribution of C_3N_4 layers. Using hydrothermal process, positively charged CNNSs and negatively charged oxidized CNTs created 3D composite (Figure 12). Due to the large work function and excellent electron conductivity of CNTs, a high nitrogen content, and porous structure, these hybrid structures exhibit rapid transfer of photoelectrons and mass, improved H_2 evolution, and stable water-splitting ability.^[129] Consequently, the migration rate of photoelectrons, separation of charges, and overall efficiency of charge carriers in C_3N_4 are enhanced. Also, it should be acknowledged here that when producing this 3D $g\text{-C}_3\text{N}_4$ NS–CNT structure, the inherent structural properties of $g\text{-C}_3\text{N}_4$ and CNTs are not compromised. These hybrid structures could be readily used for the electrocatalytic oxygen evolution reaction.

Chen's group also synthesized $g\text{-C}_3\text{N}_4/\text{CNT}$ structures using cyanamide as a precursor. The structural features, porosity, and BET surface area of the original materials were well retained, improved photocatalytic activity for H_2 evolution under visible light was also observed.^[9] The photocatalytic activity was monitored using photocurrent measurement techniques and steady/time-resolved photoluminescence spectroscopy. The findings showed that the superior properties are attributed to the amazing compatibility between $g\text{-C}_3\text{N}_4$ and conjugated CNTs. The CNT conjugates were found to boost the durability of charge carriers, control the population of temporary charge carriers, as well as boost the concentration of permanent ones. Due to this, the overall quantum efficiency is increased. CNT loading

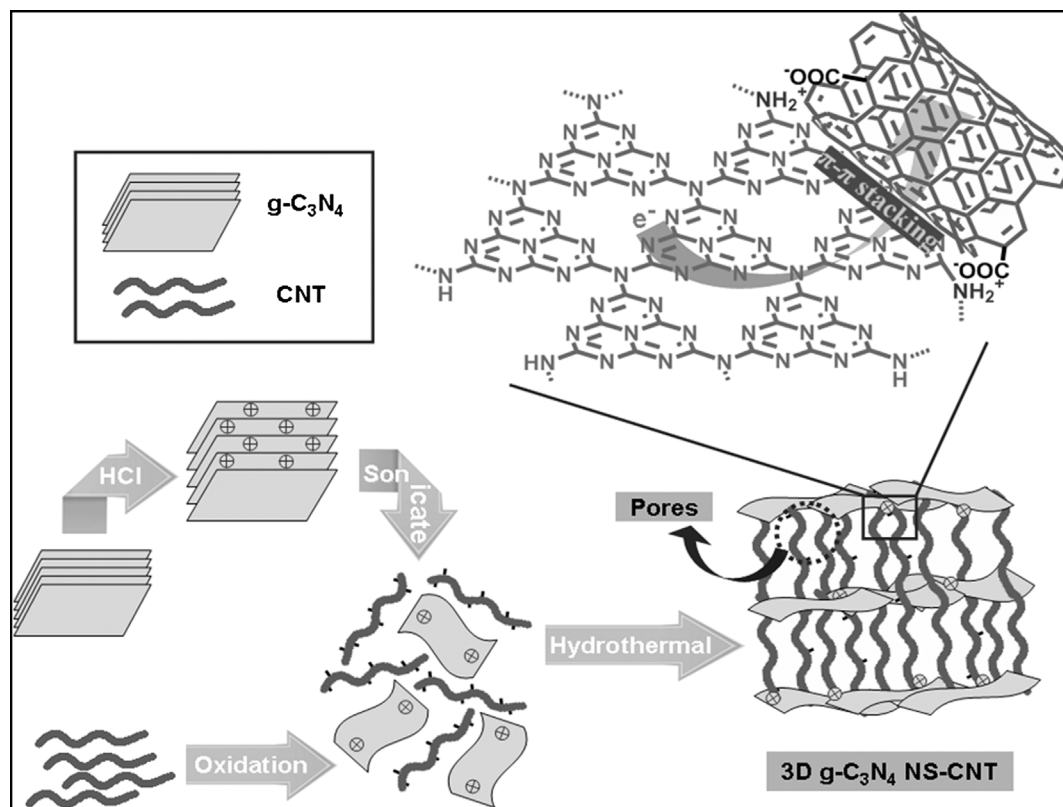


Figure 12. Preparation of the 3D $g\text{-C}_3\text{N}_4$ NS–CNT porous composite. Reproduced with permission.^[128] Copyright 2014, Wiley-VCH GmbH.

of approximately 0.2 wt% revealed the best results, i.e., H₂ production rate of 39.4 mmol h⁻¹.

5.4. g-C₃N₄/Graphene Hybrid Structures

The application of pristine g-C₃N₄ is limited due to its unimpressive electronic conductivity and photocatalytic activity. As a solution to this problem, g-C₃N₄ can be combined with graphene—a material having a similar 2D planar structure. Graphene is a 2D sheet of sp²-hybridized conjugated carbons, which acts as a building block for all significant graphitic materials (0D–3D). The desired properties of graphene include high thermal and electrical conductivity, large surface area, commendable strength, and high surface and optical properties. In g-C₃N₄/graphene hybrids, graphene can either be used as a functional component or as a support for immobilized g-C₃N₄. A unique blend of properties can be achieved by processing g-C₃N₄ with graphene into hybrid structures. With its large specific surface area and high surface conductivity, graphene promotes the transfer of charges and separation of electrons and holes, making the hybrid an attractive material for energy storage and conversion applications, such as photo-oxidation, photo- and electrocatalytic evolution of hydrogen, electrocatalytic oxygen evolution reaction, fuel cells, and Li-ion batteries.^[10]

Several methodologies have been adopted for the preparation of g-C₃N₄/graphene hybrids, including thermal, solvothermal, and other physicochemical reactions. Zhao et al.^[10] presented a brief review of the synthetic strategies for these materials. Furthermore, a dual-mesh structure that involved selective growth of 2D mesoporous g-C₃N₄ meshes on 2D mesoporous graphene meshes (g-CN@G MMs) locally was synthesized.^[130] The continuous mesh-on-mesh network was full of edges and defects, which facilitated rapid electron and mass transfer via multiple channels and provided active sites for hydrogen bonds. Due to these advantageous features, g-CN@G MMs exhibited extraordinary hydrogen evolution reactivity and durability, which rivalled most nonmetal and even some metallic catalysts.

Similarly, a unique metal-free hybrid catalyst by combining g-C₃N₄ with nitrogen-doped graphene quantum dots (N-GQDs) was prepared.^[131] In comparison with pure g-C₃N₄, this N-GQDs/g-C₃N₄ catalyst exhibited superior photocatalytic activity for hydrogen generation from the splitting of H₂O.

As it is mentioned in the section about g-C₃N₄-based hierarchical structures, g-C₃N₄ can be formed and combined with various materials such as CNTs and graphene. The large work function and enhanced electronic conductivity of g-C₃N₄/CNTs structure improve the H₂ evolution ability of g-C₃N₄. Although various g-C₃N₄-based composite structures have shown improved properties and structures, there are some features that require attention. For instance, while g-C₃N₄ enhances the mechanical properties of the hydrogel, the porosity and photogenerated charge recombination are two important issues that need to be further studied.

6. Applications of g-C₃N₄

g-C₃N₄ with distinctive semiconducting properties have become the center of attention for their performance in applications

related to energy as well as the environment.^[132] However, instant electron–hole recombination in these materials decreases their efficiency and restricts their use. This recombination is delayed in carbon nitride (C₃N₄)-based nanocomposites, thus improving the efficiency.^[133] Being sustainable, inexpensive, stable, and metal-free makes C₃N₄ materials extremely attractive for photocatalytic applications, however, it is worth mentioning that combining g-C₃N₄ with other sorts of nanoparticles widen their usage field from photocatalysis to sensing, bioimaging, novel solar energy exploitation including photocatalytic coenzyme regeneration, templating, and carbon nitride-based devices.^[134] Although g-C₃N₄ has been extensively used in solar-to-energy applications, herein, we would like to take the attention of the readers to less-studied areas such as environmental and sensing applications, and some of these applications are concisely discussed in this part.

6.1. Environmental Applications

Wide-ranging water pollution, mostly caused by clothing, food-service, and automobile industries, has worsened water body contamination around the world.^[135] Therefore, innovative methods are required for treatment of water and detection and filtration of nonbiodegradable materials.

Due to the fact that g-C₃N₄ compounds are nature-friendly, scientists are interested in exploring their photocatalytic properties for water treatment and contaminant degradation or adsorption. However, low surface area, high recombination rate of charge carriers, and inadequate light absorption of pure g-C₃N₄ make it insufficient for photocatalytic degradation. As a consequence, most of the studies are focused on producing modified C₃N₄ photocatalysts and investigating new methods such as noble metal-free doping, nonmetallic doping, and codoping of g-C₃N₄ photocatalysts for filtration of pollutants from water. As an example, the adsorption efficiency of Na-doped g-C₃N₄ synthesized by cyanamide and NaCl in removing methyl blue was studied.^[136] The maximum absorption for methyl blue of the doped material was considerably higher than the undoped one. In fact, the adsorption reached 367 mg g⁻¹, while equilibrium was reached within 1 min. It is worth mentioning that this remarkable adsorption was due to the high porosity of synthesized adsorbent. Analyses carried out illustrated that methyl blue was adsorbed on Na-doped C₃N₄ through electrostatic interactions.

Deprotonation of g-C₃N₄ using Na ions considerably improves photo reactivity as well as absorption of light.^[137] This process was conducted by heating g-C₃N₄ to 550 °C in the presence of NaCl. An increase in photocatalytic activity was attributed to the improved rate of charge transfer and optical absorption. The performed analysis revealed textural features such as the substitution of Na ions with the protons of amino functional groups and binding to atoms of nitrogen through a polymerization reaction. In another assay, an inexpensive and ecological C-g-C₃N₄/Fe₃O₄ nanocomposite was synthesized for magnetic solid-phase extraction (MSPE) of pollutants such as brominated flame retardants (BFRs) from water.^[138] The high surface area of this Taiji (an equilibrium between hydrophobicity and hydrophilicity)-principle-designed nanocomposite resulted in a maximum extraction rate of BFRs. For the aforementioned extraction

technique, the consumption rate of the solvent was found to be low, and the adsorbent was reusable. The results, such as low detection limit (limits of detection [$S/N = 3$]: 0.1–0.2 $\mu\text{g L}^{-1}$) and high recovery percentage (over the range of 92.4–99.8%) obtained from the analyses, revealed that the synthesized nanocomposite could be a great candidate for water treatment.

Metal-free black phosphorus/polymeric carbon nitride photocatalysts was prepared in *N*-methyl-2-pyrrolidone using liquid exfoliation technique displayed suitable photoactivity in the activation of oxygen reactions owing to effective charge transfer due to the desirable energy configuration.^[139] In other words, 98% of RhB was decomposed within 15 min of irradiation. The rate constant for the degradation of rhodamine B (RhB) pollutants using the 10% BP/CN composite was four times greater than that of pure carbon nitride.

A two-step method was used to synthesize phosphorus-doped $\text{g-C}_3\text{N}_4(\text{P}(x\%)\text{-g-C}_3\text{N}_4)$ by using melamine and phosphonitrilic chloride trimer ($\text{Cl}_6\text{N}_3\text{P}_3$) as precursors^[140] and the prepared $\text{P}(x\%)\text{-g-C}_3\text{N}_4$ was coated on TiO_2 nanoparticles using a solvent-thermal method to synthesize $\text{P}(x\%)\text{-g-C}_3\text{N}_4/\text{TiO}_2$ photocatalyst. Extended absorption of light along with high photocatalytic activity were some of the advantages related to the produced $\text{P}(x\%)\text{-g-C}_3\text{N}_4/\text{TiO}_2$ composite.

The results obtained by evaluating the photocatalytic activity of synthesized composite in the degradation of methyl blue under visible-light radiation revealed that $\text{P}(0.1\%)\text{-g-C}_3\text{N}_4/\text{TiO}_2$ composite offers the highest activity, which is approximately 5 times higher than that of pristine $\text{g-C}_3\text{N}_4$.^[140]

Production of phosphorus-doped porous ultrathin $\text{g-C}_3\text{N}_4$ nanosheets (PCN-S) was carried out using P element doping as well as a thermal exfoliation technique.^[141] High absorption of visible light, enhanced chemical resistance, porous surface, along with a large surface area are some advantages of PCN-S revealed by performed characterization analyses including FTIR, photocurrent response ($I-t$), XRD, TEM, and UV-vis DRS. P doping and in-plane pores of the NSs were found to have a positive impact on the photocatalytic efficiency of PCN-S on Cr (VI) reduction, as it widened the response region to light as well as increased the surface area with more active sites. The techniques utilized in this assay can motivate the preparation of $\text{g-C}_3\text{N}_4$ -based compounds having better photocatalytic performance for the degradation of other pollutants, such as 2,4-dichlorophenol.

Another technique to undertake the restrictions related to utilizing bulky $\text{g-C}_3\text{N}_4$ as photocatalysts and improving the photocatalytic activity was doping with two or more elements. In this study, melamine, ferrous chloride, and trithiocyanuric acid were calcified to synthesize Fe^{+2} and S co-doped $\text{g-C}_3\text{N}_4$.^[89] The patterns obtained by XRD analysis illustrated the similar crystal structures of the Fe (II)-doped, Fe (II)-S codoped, and pristine $\text{g-C}_3\text{N}_4$. Furthermore, the energy dispersive X-ray analysis related to Fe (II)-S codoped $\text{g-C}_3\text{N}_4$, demonstrated the dispersion of Fe and S in the high percentage of carbon and nitrogen. This study managed to achieve 91% photocatalytic degradation for the RhB dye and the degradation was enhanced by a factor of 5.4 times for the Fe(II)-S codoped $\text{g-C}_3\text{N}_4$ compared with pristine $\text{g-C}_3\text{N}_4$. In another study, Deng et al.^[142] proposed a highly optimized and proficient $\text{g-C}_3\text{N}_4$ -based photocatalyst, which was doped by O, functionalized with carbon QDs, and loaded onto

reduced graphene oxide (rGO). The photocatalyst proved to be a promising candidate for the degradation of a characteristic antibiotic, lincomycin. Due to the synergistic effect of dopant, CQDs, and rGO, the rate of degradation as well as the extent of decomposition was enhanced.

Moreover, doping of $\text{g-C}_3\text{N}_4$ by KCl was investigated and it was shown to overcome the limitations related to quick recombination of charge carriers and improves the photocatalytic efficiency in NO removal.^[143] K and Cl ions in $\text{g-C}_3\text{N}_4$ contribute to providing a double channel for electron and hole transfer. In case of KCl-doped $\text{g-C}_3\text{N}_4$, the holes in the valance band have a high capability of oxidation and the charge carriers have extended life-time due to the dual electronic channel. These unique properties increase the NO_x removal efficiency.

Introduction of potassium and phosphorus into $\text{g-C}_3\text{N}_4$ for photocatalytic H_2O_2 production under visible-light irradiation was also studied.^[144] With regards to the prepared catalyst, integrated heteroatoms increased the photogenerated charge carriers by reducing the bandgap to the visible light area. As a result, the transmission rate was increased and the recombination of the charge carriers delayed, leading to considerably higher photoactivity of catalysts. The surface-functionalized $\text{g-C}_3\text{N}_4$ was also used for phenol degradation,^[145] methyl orange degradation,^[145] oxytetracycline removal, and 2-chloroethyl ethyl sulfide degradation.

Recently, Xiao et al.^[146] presented a low-cost, high-efficiency method to produce $\text{g-C}_3\text{N}_4$ planes decorated with single Cu atoms. First, intercalation of chlorophyll sodium copper was carried out, and a supramolecular precursor was obtained. This precursor was then heated to obtain the final product. The bond between Cu atoms and compositional N (Cu-N_x) opened active channels for charge transfer, which considerably boosted the transfers of photogenerated charge carriers, both in-plane and interlayer. The proposed $\text{g-C}_3\text{N}_4$ -based catalyst was found to be highly suitable for prolonged photocatalytic evolution of hydrogen as well as for production of phenol through benzene. Table 3 shows some other environmental applications, photocatalytic activities, and features of $\text{g-C}_3\text{N}_4$ -based photocatalysts.^[78,96,145,147,90a,b] To learn more about recent advancements in energy and environmental applications of $\text{g-C}_3\text{N}_4$, the review article by Barrio et al. is highly recommended.^[148]

6.2. Sensing Applications

Although the $\text{g-C}_3\text{N}_4$ nanostructures with high surface-area-to-volume ratio are essential candidates for bioimaging and sensing, their efficiency in these fields can be improved by applying some changes in their structures through modification.^[149] Biomolecules, including heparin, glucose, along with ions such as copper, iron, chromium, and mercury are just some of the targets than could be detected by modified $\text{g-C}_3\text{N}_4$ nanocompounds.^[134a,149b] As an example, highly fluorescent $\text{g-C}_3\text{N}_4$ /quantum dots conjugation ($\text{g-C}_3\text{N}_4$ QDs) was produced through the uncomplicated ethanol-thermal treatment of bulk $\text{g-C}_3\text{N}_4$ using KOH and used in the cell membrane labeling. The synthesized $\text{g-C}_3\text{N}_4$ QDs make a great contribution to bioimaging due to its properties, such as being nontoxic, water-soluble, stable,

Table 3. g-C₃N₄-based catalysts for environmental applications.

Photocatalyst	Precursor	Application	Enhanced activity/Pristine	Surface area [m ² g ⁻¹] of Modified /Pristine	Ref.
K-doped g-C ₃ N ₄	KBr, thiourea	NO removal	0.1061 min ⁻¹ /0.0939 min ⁻¹	11/27	[147a]
K-doped g-C ₃ N ₄	KOH, DCDA	RhB degradation	0.011 min ⁻¹ /0.0017 min ⁻¹	26.9/8.9	[147b]
K-doped g-C ₃ N ₄	KI, DCDA	Phenol degradation	0.036 min ⁻¹ /0.011 min ⁻¹	–/–	[145]
Cu-doped g-C ₃ N ₄	CuCl ₂ , melamine	Methylene blue (MB) degradation	100% degradation/42% degradation	40.86/5.26	[90a]
Cu-doped g-C ₃ N ₄	CuCl ₂ , melamine	Methyl orange (MO) degradation	90.2% degradation/19.7% degradation	80.5/34.8	[147c]
Ce-doped g-C ₃ N ₄	Ce(SO ₄) ₂ ·4H ₂ O, melamine	RhB degradation	0.0155 min ⁻¹ /0.0073 min ⁻¹	18.8/11.1	[147d]
W-doped g-C ₃ N ₄	Na ₂ WO ₄ , urea, DCDA	MO degradation	0.0627 min ⁻¹ /0.0213 min ⁻¹	34.5/6.3	[90b]
Y-doped g-C ₃ N ₄	Yttrium nitrate, Urea	RhB degradation	100% degradation	103/68	[78]
Zr-doped g-C ₃ N ₄	Zirconium nitrate, Urea	RhB degradation	100% degradation/70% degradation	144.5/66.2	[147e]
C-doped g-C ₃ N ₄	Melamine, carbon foam	NO removal	0.95 min ⁻¹ / 0.25 min ⁻¹	65/11	[96]
P-doped g-C ₃ N ₄	NH ₄ PF ₆ , NH ₄ SCN	RhB degradation	0.09856 min ⁻¹ / 0.03679 min ⁻¹	–	[147f]
CeO ₂ /sulfur-doped g-C ₃ N ₄	Thiourea, cerium nitrate	MB degradation	0.0152 min ⁻¹ / 0.0044 min ⁻¹	34.9/8.9	[147g]
Graphene quantum dots decorated g-C ₃ N ₄	Phosphorus	Oxytetracycline removal	80% removal/47% removal	–	[147h]
Ag-C ₃ N ₄ -3M/CDs	Ag-C ₃ N ₄ /CDs	MB, RhB, Fuchsin, Phenol reduction and photoreduction of Cr (VI)	14.5, 34.7, 20.7, 11.6, and 40.9	19.7/14.6	[147i]
Oxidized g-C ₃ N ₄	DCDA	2-chloroethyl ethyl sulfide degradation	2.63	43/(N/A)	[147j]
g-C ₃ N ₄ nanowire (CNWs)	Cyanuric chloride–melamine	MB degradation	1.1368 h ⁻¹ /0.5367 h ⁻¹	74.25/5.30	[147k]

and biocompatible along with possessing narrow size distribution.^[150]

As subgroup J of avian leukosis viruses (ALVs-J) is of great concern in guarantying food safety, Zhou et al. designed a unique electrochemical immunosensor using mesoporous graphitic carbon nitride (mpg-C₃N₄) which could be utilized as the sensor platform to connect to the primary antibodies (Ab1).^[151] Thionine-mpg-C₃N₄ has also been recommended to be a potential electroactive probe as well as the carrier of secondary antibodies (Ab2). As compared with bulk g-C₃N₄, synthesized platform offered benefits like greater surface area and plentiful active sites. Immunosensing tests of TCID₅₀ (TCID₅₀: 50% tissue culture infective dose) were studied by differential pulse voltammetry. An increase in the reduction current was observed when the concentration of ALVs-J increased and the detection limit was estimated as 120 TCID₅₀ mL⁻¹ (Figure 13a). The effect of incubation time was studied, and the findings were used to optimize electrochemical response and current–temperature diagram. The current increased along with the increasing temperature, which was followed by a sharp decline after 37 °C (Figure 13b). Consequently, 37 °C was proposed as a suitable incubation temperature.

In another work, Prussian blue (PB) and melamine undergo a one-step pyrolysis reaction forming the graphitic carbon nitride/iron oxide in which Fe₂O₃ nanoparticles act as a protecting layer of g-C₃N₄. The features including exhibiting a longer cycle life (up to 1000 cycles) along with greater surface area, lead to greater electrochemical efficiency of synthesized composite in enzyme-free detection of glucose with a response time less than 3 s and a linear range of 2.0 × 10⁻⁶ – 2.4 × 10⁻³ mol L⁻¹.^[137]

Pt/ZnO/g-C₃N₄ composite structure was found to be a potential sensor for the detection of gases such as ethanol and NO₂.^[152] In this microwave-assisted fabrication method, exfoliated CNNs were utilized as a substrate for the growth of ZnO nanorods through bonding of Zn and N components. This was followed by Pt nanoparticle deposition, which results in the formation of Pt/ZnO/g-C₃N₄ nanostructures. This composite material was able to detect ethanol and NO₂ at 250 and 150 °C, respectively. The sensor was found to be dependent on the analyte concentration and the detection limit for ethanol and NO₂ was found as 0.072 and 0.05 ppm, respectively (Figure 14a). The Pt/ZnO/g-C₃N₄ sensor showed a temperature-dependent selectivity toward ethanol and NO₂ compared with other gases such as Cl₂, NH₃, acetone, and formaldehyde (Figure 14b).

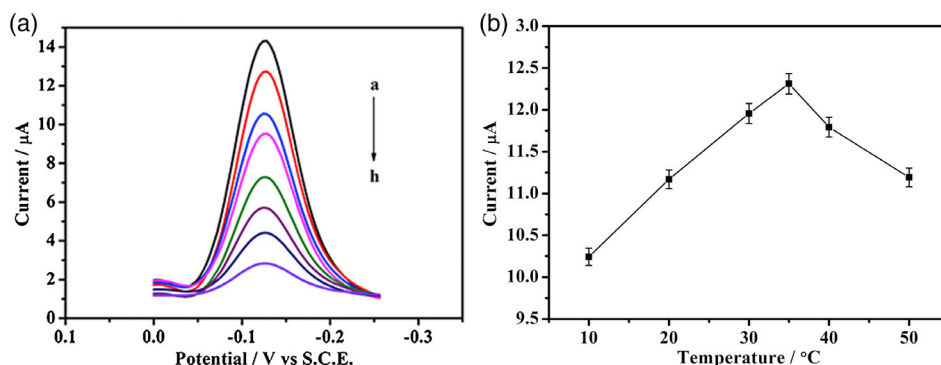


Figure 13. a) DPV responses of the immunosensor with different titers of ALVs-) under the optimized conditions, a–h: $10^{4.0}$, $10^{3.78}$, $10^{3.48}$, $10^{3.18}$, $10^{2.90}$, $10^{2.60}$, $10^{2.30}$, $10^{2.08}$ TCID₅₀/mL. b) Effects of incubation temperature of ALVs-) on DPV responses at the provided immunosensor. Adapted with permission.^[151] Copyright 2016, Elsevier.

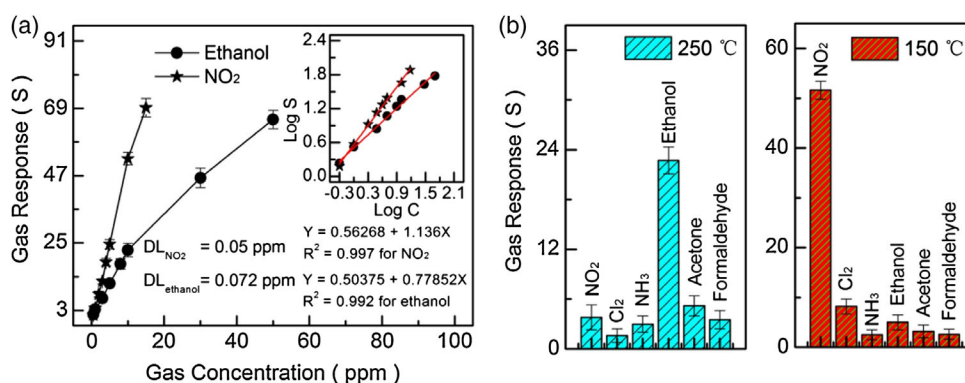


Figure 14. a) The gas response of the Pt/ZnO/g-C₃N₄ sensor at different gas concentrations and the detection limit for ethanol and NO₂. Inset: dual-logarithm of gas response (S) and gas concentration (C) for the Pt/ZnO/g-C₃N₄ sensor. b) The selectivity of the Pt/ZnO/g-C₃N₄ sensor in a gas concentration of 10 ppm at different temperatures. Adapted with permission.^[152] Copyright 2018, Elsevier.

A pyrolysis method has also been utilized to produce graphitic carbon nitride (g-C₃N₄) by melamine.^[153] In this research, the carbon paste electrode was modified by casting the g-C₃N₄/chitosan solution on the electrode. Due to the interaction between Hg (II) and CNNSSs, the sensor with high selectivity for the Hg (II) detection with a detection limit of 1.0×10^{-8} mol L⁻¹ was fabricated. It is worth mentioning that selective Hg (II) detection was achieved in the existence of other elements such as Fe (II) as well as Cu (II).

7. Conclusion

Due to its highly stable, nontoxic, metal-free, and 2D layered structure, g-C₃N₄ has emerged as a commercially significant material, especially in environmental and energy-related applications. Its impressive photocatalytic activity and ease of fabrication have attracted the attention of researchers in recent years. Various studies have explored cost-effective and green synthetic routes for g-C₃N₄ as well as methodologies to fine-tune its properties. This Review has provided a glimpse into the current developments in the synthesis, characterization, surface functionalization, and processing of g-C₃N₄.

Although g-C₃N₄ is recognized for its substantial benefits, there is still a room for improvement to utilize it to the full potential. Efforts are needed for the preparation of g-C₃N₄ with larger surface area, higher porosity, greater number of active sites, extended visible-light absorption, improved charge transport and separation, and prolonged π -conjugated build-up. The surface characteristics, which directly determines the properties of g-C₃N₄, is heavily dependent on its synthetic process, including precursors chosen, adopted polymerization temperature, time, and atmosphere. To achieve g-C₃N₄ with a superior set of qualities, it is incredibly crucial to choose the proper reaction parameters. As a precursor, urea, which can provide g-C₃N₄ with a higher rate of hydrogen evolution and better porosity, is preferred over thiourea and DCDA precursors, whereas air treatment offered the best atmosphere. As most precursors of g-C₃N₄ are earth-abundant, the production procedure is affordable. However, their low yields (<10%) is still an issue and alternative experimental procedures are in need to increase their yield.

Pristine g-C₃N₄ is not highly efficient for photocatalytic applications due to its limited physicochemical properties and needs enhancement through surface modification. However, processing techniques without using toxic reagents and precious metals would be beneficial for both cost and sustainability.

Moreover, modification at an atomic/molecular level via different covalent and noncovalent strategies detailed in this article was found to be equally fruitful. Doping and copolymerization were identified as the most common techniques in the literature, whereas framework charging of g-C₃N₄ is a rarely used technique. In fact, the tendency of covalent strategies to react with defects has shifted the focus toward noncovalent modification techniques.

For the characterization of g-C₃N₄, most researchers used XRD and SEM as tools to study g-C₃N₄ structure and morphology, respectively. Although the chemical formula of g-C₃N₄ has been widely adopted, and many crystalline carbon nitride structures are synthesized, no carbon nitride with ideal graphitic structure has been fabricated so far. Light absorption and bandgap were obtained by UV-vis analysis. The BET analysis is also critical to specify porosity and surface area information, which directly relates to active sites in photo-reactions. UV-vis and two contact methods are useful tools to characterize the conductivity and electronic structure of C₃N₄. Also, in situ characterization methods are important to investigate growth mechanism and dynamic changes. Furthermore, processing methods for g-C₃N₄ were found to have a profound effect on its overall performance. This discussion encompassed the fabrication of C₃N₄-based thin films, hydrogels, and C₃N₄-CNT and C₃N₄-graphene hybrid structures. There is still room for hybrid structures, including hybrid 2D materials with sulfides.

Designing intricate g-C₃N₄ based nanocomposites and examining the effect of semiconductors on the electronic properties of g-C₃N₄ would be two of the appealing research areas. Also, filling the existing gap in the numerical modeling of g-C₃N₄-based photocatalysts such as prediction of real electronic structure would not only enable exhaustive investigation of the performance of these photocatalysts to reduce the waste of time and resources but also make a way for new and improved photoreaction systems. Considering the widespread usage of g-C₃N₄-based materials in energy storage, water splitting for H₂ evolution, filtration, degradation of pollutants, sensing, and bio-imaging, it has become the need of the hour to increase the quantity and quality of the research work focusing on the advancement of photocatalytic performance, enrichment of properties, and optimization of the synthetic and processing methods of these materials.

Acknowledgements

C.W. and J.W.T. are thankful for financial support from UK EPSRC (EP/N009533/1), Royal Society-Newton Advanced Fellowship Grant (NA170422), and the Leverhulme Trust (RPG-2017-122).

Conflict of Interest

The authors declare no conflict of interest.

Keywords

environmental purification, functionalizations, graphitic carbon nitride, photocatalysts, sensing

Received: November 13, 2020
Revised: December 15, 2020
Published online: January 20, 2021

- [1] D. M. Teter, R. J. Hemley, *Science* **1996**, 271, 53.
- [2] Q. Lu, J. Deng, Y. Hou, H. Wang, H. Li, Y. Zhang, *Chem. Commun.* **2015**, 51, 12251.
- [3] Q. Su, J. Sun, J. Wang, Z. Yang, W. Cheng, S. Zhang, *Catal. Sci. Technol.* **2014**, 4, 1556.
- [4] X. Wang, K. Maeda, A. Thomas, K. Takane, G. Xin, J. M. Carlsson, K. Domen, M. Antonietti, *Nat. Mater.* **2009**, 8, 76.
- [5] X. Wang, S. Blechert, M. Antonietti, *ACS Catal.* **2012**, 2, 1596.
- [6] P. Praus, L. Svoboda, M. Ritz, I. Troppová, M. Šihor, K. Kočí, *Mater. Chem. Phys.* **2017**, 193, 438.
- [7] Z. Zhang, Y. Zhang, L. Lu, Y. Si, S. Zhang, Y. Chen, K. Dai, P. Duan, L. Duan, J. Liu, *Appl. Surf. Sci.* **2017**, 391, 369.
- [8] M. Mubeen, K. Deshmukh, D. R. Peshwe, S. J. Dhoble, A. D. Deshmukh, *Spectrochim. Acta, Part A* **2019**, 207, 301.
- [9] Y. Chen, J. Li, Z. Hong, B. Shen, B. Lin, B. Gao, *PCCP* **2014**, 16, 8106.
- [10] Y. Zhao, J. Zhang, L. Qu, *ChemNanoMat* **2015**, 1, 298.
- [11] L. Jiang, X. Yuan, Y. Pan, J. Liang, G. Zeng, Z. Wu, H. Wang, *Appl. Catal., B* **2017**, 217, 388.
- [12] a) S. W. Cao, J. X. Low, J. G. Yu, M. Jaroniec, *Adv. Mater.* **2015**, 27, 2150. b) W. J. Ong, L. L. Tan, Y. H. Ng, S. T. Yong, S. P. Chai, *Chem. Rev.* **2016**, 116, 7159; c) J. W. Fu, J. G. Yu, C. J. Jiang, B. Cheng, *Adv. Energy Mater.* **2018**, 8; d) Z. X. Zhou, Y. Y. Zhang, Y. F. Shen, S. Q. Liu, Y. J. Zhang, *Chem. Soc. Rev.* **2018**, 47, 2298.
- [13] S. Cao, Q. Huang, B. Zhu, J. Yu, *J. Power Sources* **2017**, 351, 151.
- [14] L. Liang, Y. Cong, F. Wang, L. Yao, L. Shi, *Diamond Relat. Mater.* **2019**, 98, 107499.
- [15] L. Yang, X. Liu, Z. Liu, C. Wang, G. Liu, Q. Li, X. Feng, *Ceram. Int.* **2018**, 44, 20613.
- [16] J. Wen, J. Xie, H. Zhang, A. Zhang, Y. Liu, X. Chen, X. Li, *ACS Appl. Mater. Interfaces* **2017**, 9, 14031.
- [17] Y. Hong, E. Liu, J. Shi, X. Lin, L. Sheng, M. Zhang, L. Wang, J. Chen, *Int. J. Hydrogen Energy* **2019**, 44, 7194.
- [18] W. Iqbal, B. Yang, X. Zhao, M. Rauf, M. Waqas, Y. Gong, J. Zhang, Y. Mao, *Catal. Sci. Technol.* **2018**, 8, 4576.
- [19] S. Yao, S. Xue, S. Peng, M. Jing, X. Qian, X. Shen, T. Li, Y. Wang, *J. Mater. Sci.: Mater. Electron.* **2018**, 29, 17921.
- [20] Y. Wang, S. Zhao, Y. Zhang, W. Chen, S. Yuan, Y. Zhou, Z. Huang, *Appl. Surf. Sci.* **2019**, 463, 1.
- [21] Z. Zhao, Y. Ma, J. Fan, Y. Xue, H. Chang, Y. Masubuchi, S. Yin, *J. Alloys Compd.* **2018**, 735, 1297.
- [22] Y. Zhang, J. Liu, G. Wu, W. Chen, *Nanoscale* **2012**, 4, 5300.
- [23] P. Niu, L. Zhang, G. Liu, H.-M. Cheng, *Adv. Funct. Mater.* **2012**, 22, 4763.
- [24] a) S. Yang, Y. Gong, J. Zhang, L. Zhan, L. Ma, Z. Fang, R. Vajtai, X. Wang, P. M. Ajayan, *Adv. Mater.* **2013**, 25, 2452; b) G. Kesavan, S.-M. Chen, *Diamond Relat. Mater.* **2020**, 108, 107975.
- [25] J. Xu, L. Zhang, R. Shi, Y. Zhu, *J. Mater. Chem. A* **2013**, 1, 14766.
- [26] A. Hatamie, F. Marahel, A. Sharifat, *Talanta* **2018**, 176, 518.
- [27] a) Y. Zheng, Y. Yang, Y. Zhang, W. Zou, Y. Luo, L. Dong, B. Gao, *Biochar* **2019**, 1, 89; b) L. Liu, M. Wang, C. Wang, *Electrochim. Acta* **2018**, 265, 275.
- [28] Z. Yang, Y. Zhang, Z. Schnepf, *J. Mater. Chem. A* **2015**, 3, 14081.
- [29] a) H. Yan, *Chem. Commun.* **2012**, 48, 3430; b) M. Peer, M. Lusardi, K. F. Jensen, *Chem. Mater.* **2017**, 29, 1496.
- [30] R. A. Fernandes, M. J. Sampaio, J. L. Faria, C. G. Silva, *RSC Adv.* **2020**, 10, 19431.
- [31] C. Zhou, R. Shi, L. Shang, L.-Z. Wu, C.-H. Tung, T. Zhang, *Nano Res.* **2018**, 11, 3462.

- [32] a) L. Zhang, H. Wang, W. Shen, Z. Qin, J. Wang, W. Fan, *J. Catal.* **2016**, *344*, 293; b) R. M. Yadav, R. Kumar, A. Aliyan, P. S. Dobal, S. Biradar, R. Vajtai, D. P. Singh, A. A. Marti, P. M. Ajayan, *New J. Chem.* **2020**, *44*, 2644; c) Q. Gu, Y. Liao, L. Yin, J. Long, X. Wang, C. Xue, *Appl. Catal., B* **2015**, *165*, 503; d) Y.-H. Xu, G. Xu, M.-Y. Sun, K. Wang, *Chem. Pap.* **2020**, *74*, 4067; e) C.-C. Hu, M.-S. Wang, W.-Z. Hung, *Chem. Eng. Sci.* **2017**, *167*, 1; f) C. Li, X. Yang, B. Yang, Y. Yan, Y. Qian, *Mater. Chem. Phys.* **2007**, *103*, 427; g) Y. Wang, F. Wang, Y. Zuo, X. Zhang, L.-F. Cui, *Mater. Lett.* **2014**, *136*, 271; h) H. Dai, X. Gao, E. Liu, Y. Yang, W. Hou, L. Kang, J. Fan, X. Hu, *Diamond Relat. Mater.* **2013**, *38*, 109.
- [33] J. Bian, C. Huang, R.-Q. Zhang, *ChemSusChem* **2016**, *9*, 2723.
- [34] a) P. Niu, G. Liu, H.-M. Cheng, *J. Phys. Chem. C* **2012**, *116*, 11013; b) P. Niu, L. C. Yin, Y. Q. Yang, G. Liu, H. M. Cheng, *Adv. Mater.* **2014**, *26*, 8046; c) J. Barrio, A. Grafmüller, J. Tzadikov, M. Shalom, *Appl. Catal., B* **2018**, *237*, 681.
- [35] H. Yu, R. Shi, Y. Zhao, T. Bian, Y. Zhao, C. Zhou, G. I. N. Waterhouse, L.-Z. Wu, C.-H. Tung, T. Zhang, *Adv. Mater.* **2017**, *29*, 1605148.
- [36] M. Green, Z. Liu, R. Smedley, H. Nawaz, X. Li, F. Huang, X. Chen, *Mater. Today Phys.* **2018**, *5*, 78.
- [37] J. Oh, J. M. Lee, Y. Yoo, J. Kim, S.-J. Hwang, S. Park, *Appl. Catal., B* **2017**, *218*, 349.
- [38] Y. Zheng, Z. Zhang, C. Li, S. Proulx, *Mater. Res. Bull.* **2016**, *84*, 46.
- [39] D. J. Martin, K. Qiu, S. A. Shevlin, A. D. Handoko, X. Chen, Z. Guo, J. Tang, *Angew. Chem. Int. Ed.* **2014**, *53*, 9240.
- [40] N. Hellgren, R. T. Haasch, S. Schmidt, L. Hultman, I. Petrov, *Carbon* **2016**, *108*, 242.
- [41] a) M. Kawasaki, K. Sompetch, T. Sarakonsri, M. Shiojiri, *Mater. Charact.* **2015**, *110*, 60; b) H. Tian, H. Fan, J. Ma, L. Ma, G. Dong, *Electrochim. Acta* **2017**, *247*, 787.
- [42] Y. T. Yew, C. S. Lim, A. Y. S. Eng, J. Oh, S. Park, M. Pumera, *ChemPhysChem* **2016**, *17*, 481.
- [43] J. Sun, J. Xu, A. Grafmueller, X. Huang, C. Liedel, G. Algara-Siller, M. Willinger, C. Yang, Y. Fu, X. Wang, M. Shalom, *Appl. Catal., B* **2017**, *205*, 1.
- [44] J. Barrio, L. Lin, X. Wang, M. Shalom, *ACS Sustainable Chem. Eng.* **2018**, *6*, 519.
- [45] J. Barrio, M. Shalom, *ACS Appl. Mater. Interfaces* **2018**, *10*, 39688.
- [46] Y. Zhao, T. Zhang, *Sci. Bull.* **2020**, *65*, 1055.
- [47] L. Zhang, R. Long, Y. Zhang, D. Duan, Y. Xiong, Y. Zhang, Y. Bi, *Angew. Chem. Int. Ed.* **2020**, *59*, 6224.
- [48] S. Chattopadhyay, S. G. Kwon, E. V. Shevchenko, J. T. Miller, S. M. Heald, in *In-Situ Characterization Techniques For Nanomaterials*, (Eds: C. S. S. R. Kumar), Springer-Verlag GmbH, Berlin **2018**, Ch. 5.
- [49] A. Azoulay, J. Barrio, J. Tzadikov, M. Volokh, J. Albero, C. Gervais, P. Amo-Ochoa, H. García, F. Zamora, M. Shalom, *J. Mater. Chem. A* **2020**, *8*, 8752.
- [50] J. Barrio, L. Lin, P. Amo-Ochoa, J. Tzadikov, G. Peng, J. Sun, F. Zamora, X. Wang, M. Shalom, *Small* **2018**, *14*, 1800633.
- [51] a) J. Liu, H. Xu, J. Yan, J. Huang, Y. Song, J. Deng, J. Wu, C. Ding, X. Wu, S. Yuan, H. Li, *J. Mater. Chem. A* **2019**, *7*, 18906; b) Y. Wang, D. Meng, X. Zhao, *Appl. Catal., B* **2020**, *273*, 119064.
- [52] J. Qin, S. Wang, H. Ren, Y. Hou, X. Wang, *Appl. Catal., B* **2015**, *179*, 1.
- [53] M. Shen, L. Zhang, M. Wang, J. Tian, X. Jin, L. Guo, L. Wang, J. Shi, *J. Mater. Chem. A* **2019**, *7*, 1556.
- [54] P. Xia, B. Cheng, J. Jiang, H. Tang, *Appl. Surf. Sci.* **2019**, *487*, 335.
- [55] C. Zhao, Z. Chen, J. Xu, Q. Liu, H. Xu, H. Tang, G. Li, Y. Jiang, F. Qu, Z. Lin, X. Yang, *Appl. Catal., B* **2019**, *256*, 117867.
- [56] a) S. A. Hodge, M. K. Bayazit, K. S. Coleman, M. S. P. Shaffer, *Chem. Soc. Rev.* **2012**, *41*, 4409; b) A. J. Clancy, M. K. Bayazit, S. A. Hodge, N. T. Skipper, C. A. Howard, M. S. P. Shaffer, *Chem. Rev.* **2018**, *118*, 7363.
- [57] A. J. Clancy, J. Melbourne, M. S. P. Shaffer, *J. Mater. Chem. A* **2015**, *3*, 16708.
- [58] M. K. Bayazit, *J. Mater. Res.* **2020**, *35*, 1472.
- [59] J. Jia, E. R. White, A. J. Clancy, N. Rubio, T. Suter, T. S. Miller, K. McColl, P. F. McMillan, V. Brázdová, F. Corà, C. A. Howard, R. V. Law, C. Mattevi, M. S. P. Shaffer, *Angew. Chem. Int. Ed.* **2018**, *130*, 12838.
- [60] X.-H. Song, L. Feng, S.-L. Deng, S.-Y. Xie, L.-S. Zheng, *Adv. Mater. Interfaces* **2017**, *4*, 1700339.
- [61] J. Oh, R. J. Yoo, S. Y. Kim, Y. J. Lee, D. W. Kim, S. Park, *Chem. Eur. J.* **2015**, *21*, 6241.
- [62] L. Yang, J. Huang, L. Shi, L. Cao, Q. Yu, Y. Jie, J. Fei, H. Ouyang, J. Ye, *Appl. Catal., B* **2017**, *204*, 335.
- [63] Y. Wang, M. K. Bayazit, S. J. A. Moniz, Q. Ruan, C. C. Lau, N. Martsinovich, J. Tang, *Energy Environ. Sci.* **2017**, *10*, 1643.
- [64] M. K. Bayazit, K. S. Coleman, *J. Am. Chem. Soc.* **2009**, *131*, 10670.
- [65] M. Quintana, K. Spyrou, M. Grzelczak, W. R. Browne, P. Rudolf, M. Prato, *ACS Nano* **2010**, *4*, 3527.
- [66] P. Zhang, H. Li, Y. Wang, *Chem. Commun.* **2014**, *50*, 6312.
- [67] X. Chen, H. Chen, J. Guan, J. Zhen, Z. Sun, P. Du, Y. Lu, S. Yang, *Nanoscale* **2017**, *9*, 5615.
- [68] J. Sun, R. Phatake, A. Azoulay, G. Peng, C. Han, J. Barrio, J. Xu, X. Wang, M. Shalom, *Chem. Eur. J.* **2018**, *24*, 14921.
- [69] a) B. K. Shrestha, R. Ahmad, S. Shrestha, C. H. Park, C. S. Kim, B. V. K. J. Schmidt, W. Zhu, X. Yuan, H. Huo, J. Gong, M. Antonietti, *Angew. Chem. Int. Ed.* **2019**, *58*, 14549; c) P. Praveena, M. Sheril Ann, S. Dhanavel, D. Kalpana, T. Maiyalagan, V. Narayanan, A. Stephen, *J. Mater. Sci.: Mater. Electron.* **2019**, *30*, 8736.
- [70] X. Fan, L. Zhang, M. Wang, W. Huang, Y. Zhou, M. Li, R. Cheng, J. Shi, *Appl. Catal. B* **2016**, *182*, 68.
- [71] Q. Cao, B. Kumru, M. Antonietti, B. V. K. J. Schmidt, *Mater. Horiz.* **2020**, *7*, 762.
- [72] J. Barrio, M. Shalom, *ChemCatChem* **2018**, *10*, 5573.
- [73] C. Zhou, C. Lai, D. Huang, G. Zeng, C. Zhang, M. Cheng, L. Hu, J. Wan, W. Xiong, M. Wen, X. Wen, L. Qin, *Appl. Catal., B* **2018**, *220*, 202.
- [74] Z. Wang, M. Chen, Y. Huang, X. Shi, Y. Zhang, T. Huang, J. Cao, W. Ho, S. C. Lee, *Appl. Catal., B* **2018**, *239*, 352.
- [75] S. Guo, Z. Deng, M. Li, B. Jiang, C. Tian, Q. Pan, H. Fu, *Angew. Chem. Int. Ed.* **2016**, *55*, 1830.
- [76] Y. Guo, S. Chu, S. Yan, Y. Wang, Z. Zou, *Chem. Commun.* **2010**, *46*, 7325.
- [77] S. Zhao, T. Guo, X. Li, T. Xu, B. Yang, X. Zhao, *Appl. Catal., B* **2018**, *224*, 725.
- [78] Y. Wang, Y. Li, X. Bai, Q. Cai, C. Liu, Y. Zuo, S. Kang, L. Cui, *Catal. Commun.* **2016**, *84*, 179.
- [79] C. D. Windle, A. Wiczorek, L. Xiong, M. Sachs, C. Bozal-Ginesta, H. Cha, J. K. Cockcroft, J. Durrant, J. Tang, *Chem. Sci.* **2020**, *11*, 8425.
- [80] Q. Cao, B. Kumru, M. Antonietti, B. V. K. J. Schmidt, *Macromolecules* **2019**, *52*, 4989.
- [81] W. Sheng, W. Li, D. Tan, P. Zhang, E. Zhang, E. Sheremet, B. V. K. J. Schmidt, X. Feng, R. D. Rodriguez, R. Jordan, I. Amin, *ACS Appl. Mater. Interfaces* **2020**, *12*, 9797.
- [82] B. Kumru, J. Barrio, J. Zhang, M. Antonietti, M. Shalom, B. V. K. J. Schmidt, *ACS Appl. Mater. Interfaces* **2019**, *11*, 9462.
- [83] Y. Zhang, C. Ren, Y. Zhang, W. Lin, K. Ding, *Appl. Surf. Sci.* **2019**, *478*, 119.
- [84] M. T. Alotaibi, *J. Mol. Struct.* **2020**, *1214*, 128192.
- [85] J. Qin, J. Huo, P. Zhang, J. Zeng, T. Wang, H. Zeng, *Nanoscale* **2016**, *8*, 2249.

- [86] D. Yuan, J. Ding, J. Zhou, L. Wang, H. Wan, W.-L. Dai, G. Guan, *J. Alloys Compd.* **2018**, 762, 98.
- [87] Y. Wang, X. Liu, X. Han, R. Godin, J. Chen, W. Zhou, C. Jiang, J. F. Thompson, K. B. Mustafa, S. A. Shevlin, J. R. Durrant, Z. Guo, J. Tang, *Nat. Commun.* **2020**, 11, 2531.
- [88] J. Wu, C. Li, H. Dong, H. Zhang, J. Han, L. Wang, S. Yu, Y. Wang, *Renewable Energy* **2020**, 157, 660.
- [89] H. Dou, S. Zheng, Y. Zhang, *RSC Adv.* **2018**, 8, 7558.
- [90] a) J. Gao, J. Wang, X. Qian, Y. Dong, H. Xu, R. Song, C. Yan, H. Zhu, Q. Zhong, G. Qian, J. Yao, *J. Solid State Chem.* **2015**, 228, 60; b) X. Rong, F. Qiu, J. Rong, X. Zhu, J. Yan, D. Yang, *Mater. Lett.* **2016**, 164, 127; c) Y. Wang, Y. Xu, Y. Wang, H. Qin, X. Li, Y. Zuo, S. Kang, L. Cui, *Catal. Commun.* **2016**, 74, 75.
- [91] S. Hu, F. Li, Z. Fan, F. Wang, Y. Zhao, Z. Lv, *Dalton Trans.* **2015**, 44, 1084.
- [92] D. Das, D. Banerjee, B. Das, N. S. Das, K. K. Chattopadhyay, *Mater. Res. Bull.* **2017**, 89, 170.
- [93] M. Fronczak, K. Demby, P. Strachowski, M. Strawski, M. Bystrzejewski, *Langmuir* **2018**, 34, 7272.
- [94] X.-X. Fang, L.-B. Ma, K. Liang, S.-J. Zhao, Y.-F. Jiang, C. Ling, T. Zhao, T.-Y. Cheang, A.-W. Xu, *J. Mater. Chem. A* **2019**, 7, 11506.
- [95] K. Wang, Q. Li, B. Liu, B. Cheng, W. Ho, J. Yu, *Appl. Catal., B* **2015**, 176–177, 44.
- [96] Z. Zhao, Y. Sun, F. Dong, Y. Zhang, H. Zhao, *RSC Adv.* **2015**, 5, 39549.
- [97] J. Fang, H. Fan, M. Li, C. Long, *J. Mater. Chem. A* **2015**, 3, 13819.
- [98] X. She, L. Liu, H. Ji, Z. Mo, Y. Li, L. Huang, D. Du, H. Xu, H. Li, *Appl. Catal., B* **2016**, 187, 144.
- [99] S. Thaweesak, S. Wang, M. Lyu, M. Xiao, P. Peerakiatkhajohn, L. Wang, *Dalton Trans.* **2017**, 46, 10714.
- [100] Y. Wang, Y. Di, M. Antonietti, H. Li, X. Chen, X. Wang, *Chem. Mater.* **2010**, 22, 5119.
- [101] Q. Han, C. Hu, F. Zhao, Z. Zhang, N. Chen, L. Qu, *J. Mater. Chem. A* **2015**, 3, 4612.
- [102] M. Ghashghaee, Z. Azizi, M. Ghambarian, *J. Phys. Chem. Solids* **2020**, 141, 109422.
- [103] N. Tian, Y. Zhang, X. Li, K. Xiao, X. Du, F. Dong, G. I. N. Waterhouse, T. Zhang, H. Huang, *Nano Energy* **2017**, 38, 72.
- [104] J. Bai, P. Zhou, P. Xu, Y. Deng, Q. Zhou, *Ceram. Int.* **2020**.
- [105] J. Zhao, L. Ma, H. Wang, Y. Zhao, J. Zhang, S. Hu, *Appl. Surf. Sci.* **2015**, 332, 625.
- [106] L. Li, M. Liang, J. Huang, S. Zhang, Y. Liu, F. Li, *Environ. Sci. Pollut. Res.* **2020**, 27, 29391.
- [107] H. Ma, Y. Li, S. Li, N. Liu, *Appl. Surf. Sci.* **2015**, 357, 131.
- [108] S. Hu, L. Ma, Y. Xie, F. Li, Z. Fan, F. Wang, Q. Wang, Y. Wang, X. Kang, G. Wu, *Dalton Trans.* **2015**, 44, 20889.
- [109] P. Babu, S. Mohanty, B. Naik, K. Parida, *ACS Appl. Energy Mater.* **2018**, 1, 5936.
- [110] Y. Yang, H. Jin, C. Zhang, H. Gan, F. Yi, H. Wang, *J. Alloys Compd.* **2020**, 821, 153439.
- [111] J. Bian, Q. Li, C. Huang, J. Li, Y. Guo, M. Zaw, R.-Q. Zhang, *Nano Energy* **2015**, 15, 353.
- [112] J. Xu, T. J. K. Brenner, L. Chabanne, D. Neher, M. Antonietti, M. Shalom, *J. Am. Chem. Soc.* **2014**, 136, 13486.
- [113] G. Peng, L. Xing, J. Barrio, M. Volokh, M. Shalom, *Angew. Chem. Int. Ed.* **2018**, 57, 1186.
- [114] J. Liu, H. Wang, Z. P. Chen, H. Moehwald, S. Fiechter, R. van de Krol, L. Wen, L. Jiang, M. Antonietti, *Adv. Mater.* **2015**, 27, 712.
- [115] J. Xu, M. Shalom, *ACS Appl. Mater. Interfaces* **2016**, 8, 13058.
- [116] W. Xiong, F. Huang, R.-Q. Zhang, *Sustain. Energy Fuels* **2020**, 4, 485.
- [117] X. Xie, X. Fan, X. Huang, T. Wang, J. He, *RSC Adv.* **2016**, 6, 9916.
- [118] J. Zhang, M. Zhang, L. Lin, X. Wang, *Angew. Chem. Int. Ed.* **2015**, 54, 6297.
- [119] C. Li, C.-B. Cao, H.-S. Zhu, *Mater. Lett.* **2004**, 58, 1903.
- [120] M. Sima, E. Vasile, A. Sima, N. Preda, C. Logofatu, *Int. J. Hydrogen Energy* **2019**, 44, 24430.
- [121] J. Safaei, N. A. Mohamed, M. F. M. Noh, M. F. Soh, M. A. Riza, N. S. M. Mustakim, N. A. Ludin, M. A. Ibrahim, W. N. R. W. Isahak, M. A. M. Teridi, *J. Alloys Compd.* **2018**, 769, 130.
- [122] a) J. Safaei, N. A. Mohamed, M. F. Mohamad Noh, M. F. Soh, N. A. Ludin, M. A. Ibrahim, W. N. Roslam Wan Isahak, M. A. Mat Teridi, *J. Mater. Chem. A* **2018**, 6, 22346–22380. b) M. Volokh, G. Peng, J. Barrio, M. Shalom, *Angew. Chem. Int. Ed.* **2019**, 58, 6138–6151.
- [123] R. Tejasvi, S. Basu, *Vacuum* **2020**, 171, 108937.
- [124] J. Liu, T. An, Z. Chen, Z. Wang, H. Zhou, T. Fan, D. Zhang, M. Antonietti, *J. Mater. Chem. A* **2017**, 5, 8933.
- [125] Q. Cao, B. Kumru, M. Antonietti, B. V. K. J. Schmidt, *Mater. Horiz.* **2020**, 7, 762.
- [126] B. Ye, C. Yao, M. Yan, H. Zhang, F. Xi, J. Liu, B. Li, X. Dong, *Macromol. Mater. Eng.* **2019**, 304, 1800500.
- [127] Z. Lin, B. Yu, J. Huang, *Langmuir* **2020**, 36, 5967.
- [128] T. Y. Ma, S. Dai, M. Jaroniec, S. Z. Qiao, *Angew. Chem. Int. Ed.* **2014**, 53, 7281.
- [129] L. Song, X. Kang, S. Zhang, *Int. J. Energy Res.* **2018**, 42, 1649.
- [130] Q. Han, Z. Cheng, J. Gao, Y. Zhao, Z. Zhang, L. Dai, L. Qu, *Adv. Funct. Mater.* **2017**, 27, 1606352.
- [131] J.-P. Zou, L.-C. Wang, J. Luo, Y.-C. Nie, Q.-J. Xing, X.-B. Luo, H.-M. Du, S.-L. Luo, S. L. Suib, *Appl. Catal., B* **2016**, 193, 103.
- [132] S. Wang, D. Li, C. Sun, S. Yang, Y. Guan, H. He, *Appl. Catal., B* **2014**, 144, 885.
- [133] Z. Zhao, Y. Sun, F. Dong, *Nanoscale* **2015**, 7, 15.
- [134] a) A. Wang, C. Wang, L. Fu, W. Wong-Ng, Y. Lan, *Nano-Micro Lett.* **2017**, 9, 47; b) F. K. Kessler, Y. Zheng, D. Schwarz, C. Merschjann, W. Schnick, X. Wang, M. J. Bojdys, *Nat. Rev. Mater.* **2017**, 2, 17030; c) J. Liu, H. Wang, M. Antonietti, *Chem. Soc. Rev.* **2016**, 45, 2308.
- [135] S. D. Richardson, T. A. Ternes, *Anal. Chem.* **2018**, 90, 398.
- [136] M. Fronczak, M. Krajewska, K. Demby, M. Bystrzejewski, *J. Phys. Chem. C* **2017**, 121, 15756.
- [137] L. Liu, J. Wang, C. Wang, G. Wang, *Appl. Surf. Sci.* **2016**, 390, 303.
- [138] M. Wang, H. Yuan, W. Deng, W. Bi, X. Yang, *J. Chromatogr. A* **2015**, 1412, 12.
- [139] Y. Zheng, Z. Yu, H. Ou, A. M. Asiri, Y. Chen, X. Wang, *Adv. Funct. Mater.* **2018**, 28, 1705407.
- [140] Z. Li, G. Jiang, Z. Zhang, Y. Wu, Y. Han, *J. Mol. Catal. A: Chem.* **2016**, 425, 340.
- [141] Y. Deng, L. Tang, G. Zeng, Z. Zhu, M. Yan, Y. Zhou, J. Wang, Y. Liu, J. Wang, *Appl. Catal., B* **2017**, 203, 343.
- [142] Y. Deng, J. Liu, Y. Huang, M. Ma, K. Liu, X. Dou, Z. Wang, S. Qu, Z. Wang, *Adv. Funct. Mater.* **2020**, 30, 2002353.
- [143] T. Xiong, H. Wang, Y. Zhou, Y. Sun, W. Cen, H. Huang, Y. Zhang, F. Dong, *Nanoscale* **2018**, 10, 8066.
- [144] J. Tian, T. Wu, D. Wang, Y. Pei, M. Qiao, B. Zong, *Catal. Today* **2019**, 330, 171.
- [145] M. Zhang, X. Bai, D. Liu, J. Wang, Y. Zhu, *Appl. Catal., B* **2015**, 164, 77.
- [146] X. Xiao, Y. Gao, L. Zhang, J. Zhang, Q. Zhang, Q. Li, H. Bao, J. Zhou, S. Miao, N. Chen, J. Wang, B. Jiang, C. Tian, H. Fu, *Adv. Mater.* **2020**, 32, 2003082.
- [147] a) T. Xiong, W. Cen, Y. Zhang, F. Dong, *ACS Catal.* **2016**, 6, 2462; b) S. Hu, F. Li, Z. Fan, F. Wang, Y. Zhao, Z. Lv, *Dalton Trans.* **2014**, 44, 1084; c) S. Le, T. Jiang, Q. Zhao, X. Liu, Y. Li, B. Fang, M. Gong, *RSC Adv.* **2016**, 6, 38811; d) R. Jin, S. Hu, J. Gui, D. Liu, *Bull. Korean Chem. Soc.* **2015**, 36, 17; e) Y. Wang, Y. Wang, Y. Li, H. Shi, Y. Xu, H. Qin, X. Li, Y. Zuo, S. Kang, L. Cui, *Catal. Commun.* **2015**, 72, 24; f) J. Y. C. W. Z. R. Y. Z. B. Chai, *Appl. Surf. Sci.* **2016**, 4;

- g) M. Jourshabani, Z. Shariatinia, A. Badiei, *J. Colloid Interface Sci.* **2017**, *507*, 59; h) A. Yuan, H. Lei, F. Xi, J. Liu, L. Qin, Z. Chen, X. Dong, *J. Colloid Interface Sci.* **2019**, *548*, 56; i) S. Asadzadeh-Khaneghah, A. Habibi-Yangjeh, K. Nakata, *J. Photochem. Photobiol. A: Chem.* **2019**, *374*, 161; j) D. A. Giannakoudakis, M. Seredych, E. Rodríguez-Castellón, T. J. Bandoz, *ChemNanoMat* **2016**, *2*, 268; k) M. Xie, W. Wei, Z. Jiang, Y. Xu, J. Xie, *Ceram. Int.* **2016**, *42*, 4158.
- [148] J. Barrio, M. Volokh, M. Shalom, *J. Mater. Chem. A* **2020**, *8*, 11075.
- [149] a) P. Murugesan, J. A. Moses, C. Anandharamkrishnan, *J. Mater. Sci.* **2019**, *54*, 12206; b) W. K. Darkwah, Y. Ao, *Nanoscale Res. Lett.* **2018**, *13*.
- [150] Y. Zhan, Z. Liu, Q. Liu, D. Huang, Y. Wei, Y. Hu, X. Lian, C. Hu, *New J. Chem.* **2017**, *41*, 3930.
- [151] D. Zhou, M. Wang, J. Dong, S. Ai, *Electrochim. Acta* **2016**, *205*, 95.
- [152] H. Tian, H. Fan, J. Ma, Z. Liu, L. Ma, S. Lei, J. Fang, C. Long, *J. Hazard. Mater.* **2018**, *341*, 102.
- [153] M. Amiri, H. Salehniya, A. Habibi-Yangjeh, *Ind. Eng. Chem. Res.* **2016**, *55*, 8114.



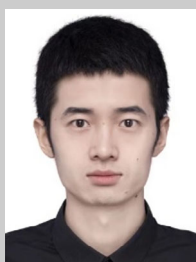
Tuçe Fidan is a master student in materials science and nanoengineering at Sabancı University, Turkey. She graduated from the Department of Materials Science and Nanotechnology Engineering, TOBB University of Economics and Technology, Turkey. She is currently working on the synthesis, characterization, and surface functionalization of graphitic carbon nitride for photocatalytic hydrogen production.



Milad Torabfam received his bachelor's degree in bioengineering from Sahand University of Science, Iran, in 2013. He completed his master's studies at the same university, in 2016. He is currently a Ph.D. candidate (Material Science Program) at Sabancı University.



Qandeel Saleem is a graduate student within the material science and nanoengineering program at Sabancı University, Turkey. She has received her bachelor's degree in metallurgical engineering from NED University of Engineering & Tech, Pakistan. Currently, she is working as a part of NanoChemCom – Dr. M.K. Bayazit's research group at Sabancı University Nanotechnology Research and Application Center (SUNUM).



Chao Wang did his B.Sc. and M.Sc. degrees at Northwestern Polytechnical University. He is currently a Ph.D. student in the Solar Energy & Advanced Materials Research Group at UCL, under supervision of Prof. Junwang Tang. His current research study mainly focuses on photocatalytic conversion of methane into value added chemicals.



Hasan Kurt obtained his Ph.D. in materials science and engineering from Sabancı University in 2016. Later, he joined the Department of Biomedical Engineering in Istanbul Medipol University as a faculty member. His research is focused on light-matter interactions and exploitation of surface plasmons in various applications such as light management in optoelectronics devices, plasmonics biosensing, and organic photovoltaics. Since 2014, he also holds the position of managing partner of the tech start-up company, Nanosolar Plasmonics Ltd., focusing on commercial plasmonics biosensor platforms.



Meral Yüce received her Ph.D. in biotechnology from the Institute of Biotechnology, Ankara University, Turkey, in 2011. Her professional research career started in 2011 at SUNUM, focusing on analytical method development for low-cost and robust biosensor platforms. She was a visiting scientist at the Institute of Biotechnology and Chemical Engineering of Cambridge University, UK (2010-2011), and at MonoJO Antibody Production Company, Jordan (2010-2011). She also conducted complementary research at Leeds University, UK (2012-2013) as a British Council Fellow and at Imperial College London (2017) as an EMBO-ST Fellow.



Junwang Tang is a Fellow of European Academy of Sciences, Fellow of the Royal Society of Chemistry and professor of materials chemistry and engineering at the Department of Chemical Engineering at University College London. His research interests encompass photocatalytic small molecule activation (eg. CH₄, N₂, H₂O, and CO₂) and microwave catalysis (e.g., plastic recycling), together with investigation of the underlying charge dynamics and kinetics by state-of-the-art spectroscopies. In parallel, he explores the design of the chemical reactors for the above-mentioned processes.



Mustafa K. Bayazit completed his Ph.D., in 2010, at the University of Durham, UK, on carbon nanomaterials. He then worked at Imperial College London and University College London as a researcher for eight years. In 2019, he joined the SUNUM as a principal investigator. His current work involves the surface functionalization of 2D nanomaterials for energy, environmental and sensing applications, and microwave-intensified fluidic systems for continuous manufacturing. He currently holds the 2232-International Fellowship for Outstanding Researchers.